

Spectral signatures of non-trivial topology in a superconducting circuit

L. Peyruchat, R. H. Rodriguez, J.-L. Smirr, and Ç. Ö. Girit*
*Quantronics Group, Université Paris Saclay, CEA,
 CNRS, SPEC, 91191 Gif-sur-Yvette Cedex, France and
 Φ₀, JEIP, USR 3573 CNRS, Collège de France, PSL University,
 11, place Marcelin Berthelot, 75231 Paris Cedex 05, France*

R. Leone
*Laboratoire de Physique et Chimie Théoriques, Université de Lorraine,
 CNRS, F-54506 Vandœuvre lès Nancy Cedex, France*
 (Dated: January 30, 2024)

Topology, like symmetry, is a fundamental concept in understanding general properties of physical systems. In condensed matter systems, non-trivial topology may manifest itself as singular features in the energy spectrum or the quantization of observable quantities such as electrical conductance and magnetic flux. Using microwave spectroscopy, we show that a superconducting circuit with three Josephson tunnel junctions in parallel can possess energy degeneracies indicative of *intrinsic* non-trivial topology. We identify three topological invariants, one of which is related to a hidden quantum mechanical supersymmetry. Depending on fabrication parameters, devices are gapless or not, and fall on a simple phase diagram which is shown to be robust to perturbations including junction imperfections, asymmetry, and inductance. Josephson tunnel junction circuits, which are readily fabricated with conventional microlithography techniques, allow access to a wide range of topological systems which have no condensed matter analog. Notable spectral features of these circuits, such as degeneracies and flat bands, may be leveraged for quantum information applications.

I. INTRODUCTION

A physical system is topologically non-trivial if it has a discrete property that is robust to perturbations [1]. For example a superconducting ring is topologically non-trivial as the magnetic flux through it is quantized and conserved no matter how the ring is deformed, as long as it is not broken. The quantized transconductance of a semiconductor in the quantum Hall regime is another topological invariant [2]. Some topological invariants may be related to singular spectral features such as band crossings [3]. Many new invariants, describing different kinds of topological order, have been discovered in condensed matter systems [4, 5]. In electronic systems the topological invariants often correspond to measurable, discrete, universal electromagnetic quantities, such as flux (h/e), charge (e), or resistance (h/e^2) [6]. Both topological spectral features and quantized transport parameters find applications in fields such as metrology [7] and quantum information [8].

Although topological phases in materials arise from symmetries of many-particle Hamiltonians [9], simple single-particle systems with non-trivial topology also exist, such as a spin-1/2 electron in a magnetic field B , where the degeneracy at $B = 0$ gives rise to a topological charge [3, 10]. Circuits with Josephson tunnel junctions, due to their versatility, scalability, and reliability, have been used for the simulation of well known topological models [11]. But these circuits, which can often be described by a few bosonic degrees of freedom, also have

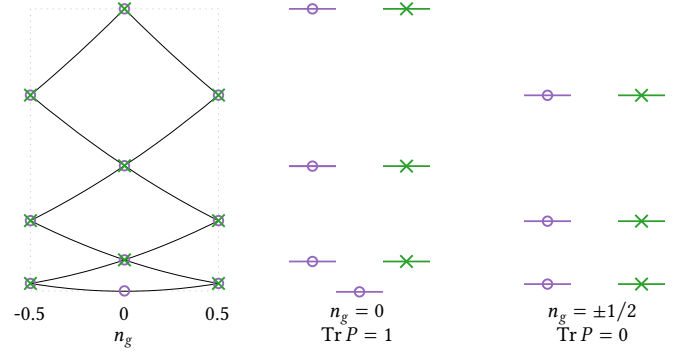


FIG. 1. Hidden quantum mechanical supersymmetry in the spectrum of the charging Hamiltonian. At charge offset $n_g = 0$ (Witten index $\text{Tr } P = 1$), supersymmetry is *unbroken*: the ground state at zero energy is not degenerate, whereas all excited states are doubly degenerate. At $n_g = \pm 1/2$ ($\text{Tr } P = 0$), supersymmetry is *broken*: the ground state energy is greater than zero and all states are doubly degenerate. “Bosonic” (even parity) and “fermionic” (odd parity) superpartners are indicated by purple circles and green crosses.

inherent topological properties. These inherent properties are derived from the real Hamiltonian, a function of the flux and charge variables [12], as opposed to a “simulated” one, and may have no analog in real materials [13–26]. We identify and measure three topological invariants in a simple superconducting circuit with three Josephson junctions in parallel, the BiSQUID. The invariants determine whether degeneracies exist (curvature invariant B); characterizes the global structure of degeneracies (Witten index $\text{Tr } P$); and associates to each degeneracy a unique winding number N_2 .

* caglar.girit@cnrs.fr

II. SUPERSYMMETRY OF CHARGING HAMILTONIAN

The first invariant we consider is the Witten index as it has been largely overlooked and pertains to a wide class of Josephson junction circuits with degeneracies. Consider the spectrum of a quantum capacitor described by the Hamiltonian $H_C = E_C(n - n_g)^2$, where $E_C = (2e)^2/2C$ is the charging energy and $2en_g$ is the offset charge [Fig. 1] [27, 28]. The eigenstates $|n\rangle$, with n integer, correspond to the number of excess Cooper pairs on the ungrounded electrode, and span the Hilbert space of 2π -periodic wavefunctions in θ , the phase difference across the capacitor. The fundamental commutation relation is $[\theta, n] = i$. The Hamiltonian H_C can also describe the flux states of a superconducting ring, a quantum rotor, or the angular momentum states of a charged particle confined to a ring [29–33].

The energy diagram Fig. 1 has a peculiar degeneracy structure: at $n_g = 0$ all states except the zero energy ground state are doubly degenerate, whereas at $n_g = \pm 1/2$, all states are degenerate. This spectral signature is reminiscent of supersymmetric quantum mechanics (SUSY QM), a toy model for SUSY quantum field theories in which a bosonic Hamiltonian is augmented with an additional fermionic “superpartner” degree-of-freedom [34–38]. The resulting generic supersymmetric Hamiltonian can either have a doubly degenerate spectrum with a zero energy ground state singlet, called *unbroken* SUSY ($n_g = 0$), or in *broken* SUSY, have a doublet non-zero energy ground state ($n_g = \pm 1/2$).

Whereas H_C has no explicit fermionic component, it has a hidden supersymmetry which generates the same superalgebra that yields the distinctive spectrum of SUSY QM models [Appendix A]. Hidden supersymmetry in quantum bosonic systems, such as the free particle [38], bound state Aharonov-Bohm problem [39, 40], and Jaynes-Cummings model [41] was discovered previously. Supersymmetry also plays a role in models such as SYK [42], is debated to exist in certain topological superconductors [43, 44] and has been measured in artificial systems such as ion trap simulators [45]. A five Josephson junction circuit with a configuration exhibiting hidden unbroken supersymmetry was also proposed [46]. Here we consider the hidden supersymmetry, both broken and unbroken, inherent in any superconducting circuit where the Hamiltonian at degeneracy is the charging Hamiltonian H_C .

The symmetry which partitions eigenstates into “bosons”, with even parity, and “fermions”, with odd parity, is inversion about the point $n = n_g$. In the charge basis, the parity operator is $P(n_g) = \sum_n | -n + 2n_g \rangle \langle n |$, defined only for $n_g = 0, \pm 1/2$ when restricted to the Hilbert space. Since $[P, H_C] = 0$ and $P^2 = 1$, energy eigenstates can also be chosen to be parity eigenstates with eigenvalues ± 1 . Combining P , referred to as a grading operator in supersymmetry, with the “supercharge” operator, $Q(n_g) = \sqrt{E_C}(n - n_g)$, we have the following

algebra,

$$P^2 = 1, \quad \{P, Q\} = 0, \quad Q^2 = H_C, \quad (1)$$

which is an equivalent definition of SUSY QM [47]. These relations imply that all non-vanishing eigenvalues of H_C are associated to degenerate eigenvectors [Appendix A] and give rise to the energy level structure of Fig. 1. It can also be shown that the degenerate doublets are Kramers pairs Appendix A. The singlet ground state at $n_g = 0$ lacks a “fermionic” partner because there is no odd parity eigenstate of zero momentum.

The Witten index, $\text{Tr } P$, counts the difference between the number of bosonic and fermionic states: 1 for unbroken SUSY ($n_g = 0$) and 0 for broken SUSY ($n_g = \pm 1/2$). $\text{Tr } P$ is ill-defined for non-integer $2n_g$ as the 2π periodicity of the wavefunctions restricts n to integer values. The curvature invariant, which dictates whether supersymmetry occurs and the Witten index can be defined, as well as the winding invariant will be defined below in the context of the design and measurement of the BiSQUID.

III. SUPERCONDUCTING TOPOLOGICAL CIRCUIT

In order to detect signatures of supersymmetry, we seek a quantum electrical circuit described by the charging Hamiltonian. A small Josephson tunnel junction, known as a Cooper pair box or charge qubit [27, 28], is quantum coherent and has a capacitance with large $E_C \gg kT$. However the Josephson coupling hybridizes the charge states, lifting the degeneracies at $n_g = 0, \pm 1/2$. By the Von Neumann-Wigner theorem [48], barring accidental degeneracies, at least three parameters are necessary to obtain band crossings in a generic Hamiltonian, whereas the Cooper pair box only has one, the gate voltage.

Adding a junction in parallel yields a superconducting quantum interference device (SQUID) or Cooper pair transistor, which has an additional variable, the magnetic flux threading the SQUID loop. A SQUID can be considered a single Josephson junction with a flux-tunable Josephson energy $E_J^*(\Phi)$. Although a completely symmetric SQUID at half a quantum flux bias ($\Phi = \Phi_0/2 = h/4e$) will have zero E_J^* , leaving only the charging Hamiltonian H_C , this requires two junctions with exactly identical critical currents which is impossible to fabricate.

Putting a third junction in parallel will result in a circuit with topologically protected degeneracies: the BiSQUID [Fig. 2] [25, 49]. Such a circuit has a flux parameter for each loop, Φ_L and Φ_R , in addition to the gate voltage n_g . For a large range of junction parameters, by tuning both magnetic fluxes through the loops one can effectively cancel out the overall Josephson coupling, leaving only the capacitive term in the Hamiltonian.

The complex effective Josephson energy of the BiSQUID is

$$E_J^*(\varphi_L, \varphi_R) = E_J (1 + \alpha e^{-i\varphi_L} + \beta e^{i\varphi_R}), \quad (2)$$

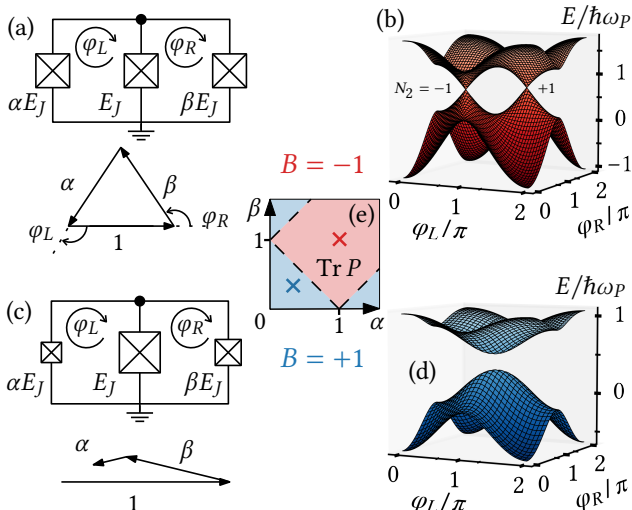


FIG. 2. (a) The BiSQUID, comprised of three Josephson tunnel junctions in parallel, acts as a single junction with an effective Josephson energy E_J^* which can be represented geometrically as the sum of three vectors of lengths $1, \alpha, \beta$ and angles φ_L, φ_R . The junction asymmetries α, β are the relative Josephson energies of the left and right junctions and φ_L, φ_R are the reduced magnetic fluxes threading each loop. The Hamiltonian reduces to the charging term H_C when $E_J^* = 0$, or equivalently the vectors form a triangle, resulting in a spectrum with a supersymmetric degeneracy structure (curvature invariant $B = -1$). (b) The two lowest energy bands for $n_g = 1/2$ (broken SUSY) are plotted as a function of φ_L, φ_R , showing ground state degeneracy at two inequivalent points identified by their winding number $N_2 = \pm 1$ and corresponding to closing the triangle clockwise or counter-clockwise. All excited states are also doubly degenerate at those points. If the Josephson energies do not satisfy the triangle inequality (c, $\alpha = \beta = 0.4$) the system is always gapped (d) ($B = +1$). Neither the ground nor excited states are degenerate. Energies are normalized by the plasma energy $\hbar\omega_p = \sqrt{2E_C E_J(1 + \alpha + \beta)}$. (e) Phase diagram as a function of junction asymmetries. Critical line (dashed) separates topologically trivial ($B = +1$, blue) and non-trivial ($B = -1$, red) regimes. When $B = -1$, the Witten index $\text{Tr } P = 0$ if SUSY is unbroken ($n_g = 0$) and $\text{Tr } P = 1$ if it is broken ($n_g = 1/2$).

where E_J is the Josephson energy of the middle junction, α and β are the Josephson energies of the left and right junction scaled to E_J , and $\varphi_{L,R} = 2\pi\Phi_{L,R}/\Phi_0$ are the reduced magnetic fluxes.

As expected for supersymmetry, the BiSQUID spectrum has a tower of degeneracies when $E_J^* = 0$ and $2n_g$ is integer. The condition $E_J^*(\varphi_L, \varphi_R) = 0$ is equivalent to the existence of a closed triangle with relative angles φ_L, φ_R and side lengths $1, \alpha$ and β . A symmetric BiSQUID ($\alpha = \beta = 1$) has an effective Josephson energy which is zero when $\varphi_R = -\varphi_L = \pm 2\pi/3$ [Fig. 2(a)], corresponding to an equilateral triangle oriented clockwise ($\varphi_R > 0$) or counterclockwise ($\varphi_R < 0$). The spectrum [Fig. 2(b)] for $n_g = 1/2$ will then have two conical band

crossings where the ground state is degenerate (broken SUSY). All excited states will also be doubly degenerate at the same diabolical points [3] in the (φ_L, φ_R) “Brillouin zone,” as shown in [Appendix Fig. 7]. When the junction asymmetry is too large, such as $\alpha + \beta < 1$ [Fig. 2(c)], it is no longer possible to close the triangle. Then the ground state is not degenerate and the spectrum has a gap [Fig. 2(d)]. For $n_g = 0$ (unbroken SUSY), which is not shown in [Fig. 2], all excited states are degenerate but the zero-energy ground state is not.

The phase diagram for the BiSQUID [Fig. 2(e)] is given by the triangle inequality $|\alpha - \beta| < 1 < \alpha + \beta$, which determines whether the triangle can be closed and there exists a solution to $E_J^*(\varphi_L, \varphi_R) = 0$ [50]. In the topologically non-trivial phase, one can have either broken or unbroken SUSY depending on the value of n_g . Unbroken SUSY ($n_g = 0$) is a gapped topologically non-trivial state whereas broken SUSY ($n_g = 1/2$) is gapless. When the triangle condition cannot be satisfied and therefore supersymmetry is not present, the system is both gapped *and* topologically trivial. The curvature invariant, described below and measured for several devices, encodes the triangle inequality and indicates whether a BiSQUID is topologically non-trivial.

Since the triangle condition can be satisfied for a range of α, β , the degeneracies at both $n_g = 0$ and $n_g = 1/2$ are robust to variations in the charging energy E_C and the three Josephson energies. The two diabolical points will move in the Brillouin zone as the junction asymmetries α and β are varied, converging at high symmetry points where φ_L and φ_R are either zero or π as the parameters approach the critical lines $|\alpha \pm \beta| = 1$. On the critical lines the greatest Josephson energy is equal to the sum of the two others and the diabolical points merge to produce an energy dispersion described by a power law.

In the analogy to a topological material, the reduced magnetic fluxes $\varphi_{L,R}$ which are odd under time-reversal play the role of k_x, k_y for a 2D crystal. The offset charge n_g is related to an electric field and therefore even under time-reversal and is considered a control parameter [25]. In the condensed matter context, the BiSQUID at $n_g = 0$ or $1/2$ is a 2D topological semimetal with time-reversal and inversion symmetry. The conical two-band crossings are referred to as either 2D Weyl points [51] or Dirac points of spinless graphene (class AI with inversion) [9, 52].

IV. EXPERIMENTAL SETUP

Spectroscopy is a direct probe of energy transitions and is well suited to detect the distinctive spectral signatures of supersymmetry. Circuit quantum electrodynamics [53] techniques are routinely used for superconducting qubit characterization and manipulation. Spectroscopy has previously been used in an ion trap quantum simulator to detect degeneracies due to supersymmetry [45].

We use a microwave cavity resonator to perform the spectroscopy of several BiSQUIDs in both trivial and topological regimes (Fig. 3). A BiSQUID (purple) is capacitively coupled to the voltage anti-node of a coplanar waveguide lambda-mode resonator (blue) with f_r approximately 7 GHz to 9 GHz and loaded quality factor $Q_L > 10^3$. We first deposit 100 nm aluminum on a silicon substrate then fabricate the resonator and control lines using photo-lithography and wet etching. The Josephson junctions of the BiSQUID are made of aluminum and are patterned using e-beam lithography and a double-angle evaporation technique. The surface area of each JJ is approximately $200 \times 200 \text{ nm}^2$ such that $E_J \approx E_C$ (see inset of Fig. 3(c)). All experiments are conducted in a dilution refrigerator at 10 mK. The transmission of the resonator at frequency f_1 is probed using a vector network analyzer, and transitions between energy levels of the BiSQUID are detected via changes in f_1 resulting from a second tone of frequency f_2 exciting the BiSQUID via a local flux line. The relevant transition matrix elements are $\langle k|\theta|j\rangle$ determining the type of spectral lines that can be resolved. Further details of the setup are provided in [Appendix E].

The charge offset n_g is controlled by applying a gate voltage $V_g = 2en_g/C_g$ to the central conductor of the DC gate voltage line, even with careful filtering of the DC gate voltage line, the value of n_g slowly drifts a few percent per hour and randomly jumps on a timescale of minutes. To compensate we repeatedly perform quick calibrations approximately every minute. We sweep V_g over a few periods while probing the resonator to find the value of V_g corresponding to the desired n_g . This allows us to correct for slow drift and detect charge jumps, in which case data is discarded and remeasured.

Quasiparticle (QP) poisoning is a large source of error for many superconducting quantum devices [54]. High-energy photons or ionizing radiation [55–59] may create non-equilibrium quasiparticles which can then tunnel to the superconducting island of the BiSQUID, shifting n_g by 0.5 (1e). Despite broadband noise filtering and superconducting gap engineering, we measured constant jumps between quasiparticle parities with a typical switching time on the order of 300 ms and average populations of 50% for each parity [Appendix F]. Post-measurement processing allows sorting the data for each QP parity.

Direct currents I_L and I_R are applied to two local flux lines (see red and green in Fig. 3) to control loop fluxes φ_L and φ_R . The second microwave tone used to excite transitions of the BiSQUID is applied via one of these flux lines. To find the conversion between applied currents (I_L, I_R) and reduced fluxes (φ_L, φ_R), we determine the unit cell for the periodic resonator shift [Fig. 4(a,b)] and compensate accordingly.

V. MEASURED SPECTRA

We fabricated several BiSQUIDs with different Josephson energy asymmetries α and β to explore the phase di-

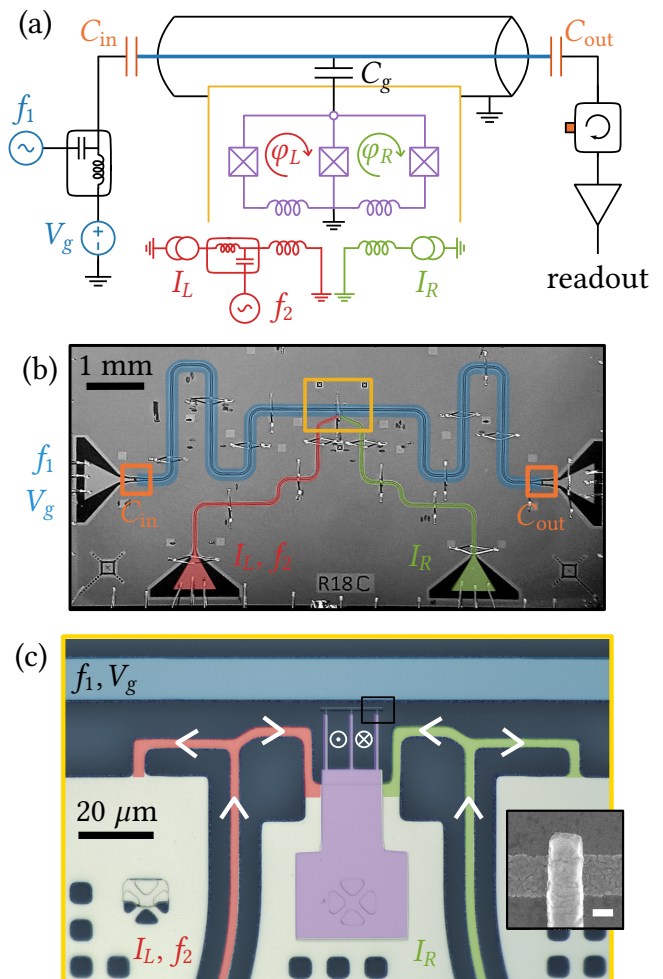


FIG. 3. Spectroscopy setup. (a) Electrical diagram of a BiSQUID (purple) capacitively coupled to the voltage anti-node of a lambda-mode coplanar waveguide resonator (blue). Gate voltage V_g and microwaves at frequency f_1 are applied to the resonator using a bias tee (left). Reduced loop fluxes φ_L and φ_R are set by direct currents I_L and I_R applied to local flux lines (red, green). A microwave drive at frequency f_2 (left flux line, red) excites transitions of the BiSQUID. (b) False-colored optical microscope image of device R18C. The resonator is made of aluminum (gray) on a silicon substrate (black). (c) Optical image of BiSQUID (yellow inset in (b)). Inset: SEM image of rightmost Josephson junction (scale bar 100 nm, junction surface area $0.034 \mu\text{m}^2$).

agram [Fig. 2(e)]. BiSQUID R17A was fabricated in the topologically trivial regime, with a middle junction about three times larger than the outer ones ($\alpha \approx \beta \approx 1/3$). Two other BiSQUIDs, R17C and R18C, were fabricated with junctions of similar area in order to be in the topologically non-trivial regime. For simplicity only the middle junction area was varied, keeping $\alpha \approx \beta$ such that degeneracies remain on the $\varphi_L = \varphi_R \equiv \varphi_{\text{diag}}$ axis. As α, β decreases from the equilateral configuration $\alpha = \beta = 1$, degeneracies should move toward each other along the

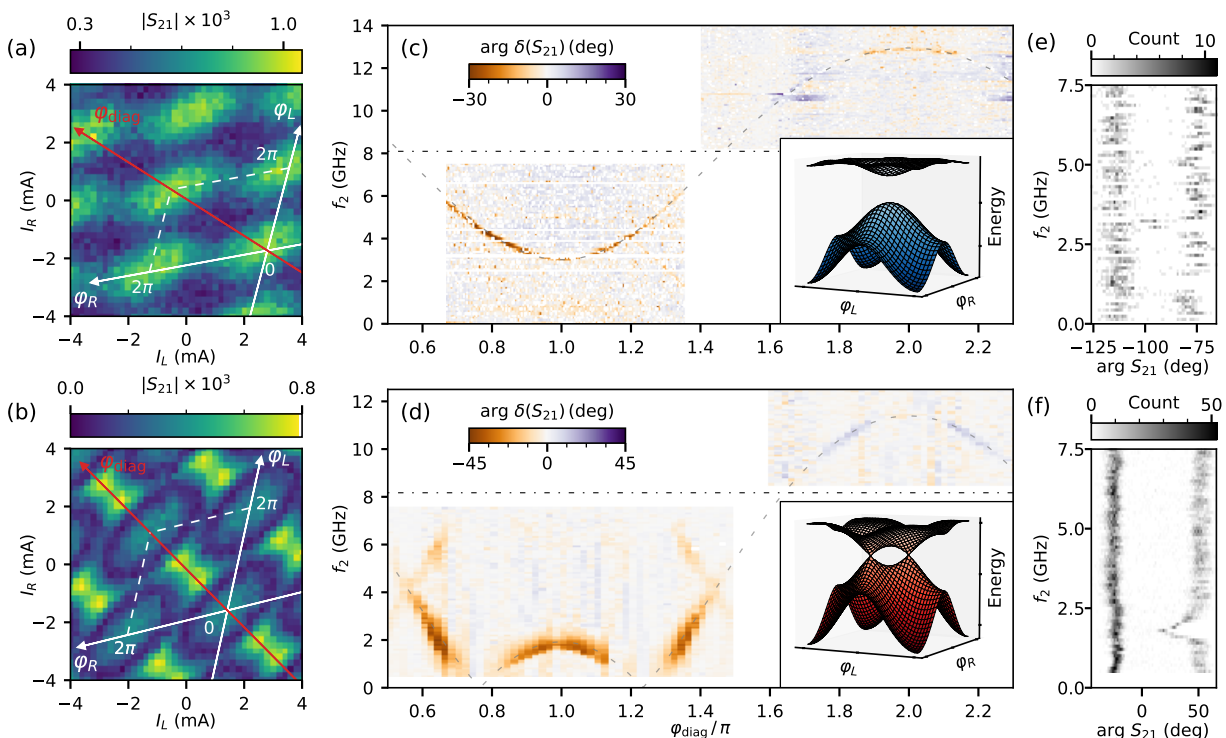


FIG. 4. Spectroscopy of topologically trivial (top row, R17A) and non-trivial (bottom row, R17C) BiSQUIDs at $n_g = 1/2$. (a,b) One-tone signal shift of resonator as a function of currents I_L, I_R in the two flux lines. Superposed are reduced flux axes φ_L and φ_R (solid white), diagonal $\varphi_{\text{diag}} = \varphi_L = \varphi_R$ (red), and unit cell (dashed). (c,d) Two-tone phase shift of resonator along φ_{diag} . Overlaid on the data are the bare frequency of each resonator (dash-dotted line) and the transition frequency f_{01} obtained from fitting to the BiSQUID Hamiltonian [Eq. (3)] (dashed lines). Insets plot first two energy levels of the Hamiltonian using fit parameters over the unit cell. (e,f) Histograms of $\arg S_{21}(f_2)$ at $\varphi_{\text{diag}} = \pi$ representative of data used to obtain spectra in (c,d). The distribution is bimodal due to quasiparticle poisoning.

φ_{diag} axis until they merge at $\varphi_{\text{diag}} = \pi$ for $\alpha = \beta = 1/2$.

A first signature of the topological phase of the BiSQUID is found in the flux maps [Fig. 4(a,b)]. The asymmetric BiSQUID R17A ($\alpha = \beta = 0.34$) shows only a single minimum (dark blue) in one unit cell [Fig. 4(a)]. On the contrary for the more symmetric device R17C ($\alpha = \beta = 0.67$) we observe two maxima (yellow). The extrema in both maps correspond to local minima of the BiSQUID transition energy. For a topologically trivial BiSQUID, such as R17A (a), the gap is smallest at $\varphi_{\text{diag}} = \pi$. For a BiSQUID in the topologically non-trivial regime, there are always two degeneracies, and thus two extrema.

We then performed two-tone spectroscopy by measuring the transmission S_{21} of the resonator in the presence of a second tone of frequency f_2 at different values of φ_{diag} . The charge offset is set to $n_g = 0.5$, where degeneracies are expected, and post-processed to account for quasiparticle poisoning. The two-tone phase shift is shown in [Fig. 4(c,d)], where the flux-dependent single-tone phase offsets have been removed. We observe one main spectroscopy line corresponding to the transition f_{01} from ground to first excited state. At $\varphi_{\text{diag}} = 2\pi$ the transition has a maximum of 12 – 13 GHz for both BiSQUIDs. However near $\varphi_{\text{diag}} = \pi$ the transition

strongly differs for the two circuits. For the BiSQUID in the trivial regime, f_{01} has a single minimum of 3 GHz near $\varphi_{\text{diag}} = \pi$ [Fig. 4(c)]. The BiSQUID in the topologically non-trivial regime shows two minima, at $\varphi_{\text{diag}} \approx 0.75\pi$ and $\varphi_{\text{diag}} \approx 1.25\pi$, and the transition has negative curvature and a local maximum at $\varphi_{\text{diag}} = 1\pi$. The f_{01} spectral line disappears below 1 GHz due to both thermal effects and because the charge-coupled resonator shift goes to zero at the degeneracy point [60].

The raw data leading to the maps [Fig. 4(c,d)] are shown for the respective devices at a flux bias $\varphi_{\text{diag}} = \pi$ in Fig. 4(e,f). Each horizontal cut is a histogram of the phase of the transmitted signal $\arg S_{21}$ at the resonator frequency obtained from multiple measurements while driving at the second tone frequency f_2 (y-axis). The color scale corresponds to the number of counts. Due to quasiparticle poisoning the distribution is bimodal, with the second, spurious, mode corresponding to a charge offset $n_g \pm 0.5 = 0$. A threshold is applied to distinguish between the two QP states, and only data corresponding to $n_g = 0.5$ is shown in Fig. 4(c,d). The desired mode, $n_g = 0.5$, shows clear shifts when f_2 is resonant with a BiSQUID transition, whereas the spurious mode is relatively constant. This is because the excitation gap near $\varphi_{\text{diag}} = \pi$ for $n_g \equiv 0$ is above approximately 8 GHz.

The transition frequencies extracted from the raw data are plotted as a function of φ_{diag} for four BiSQUID devices, R17A, R17B, R17C, and R18C in Fig. 5 (circle markers). The error bars correspond to the full-width half-max (FWHM) of the Gaussian fits.

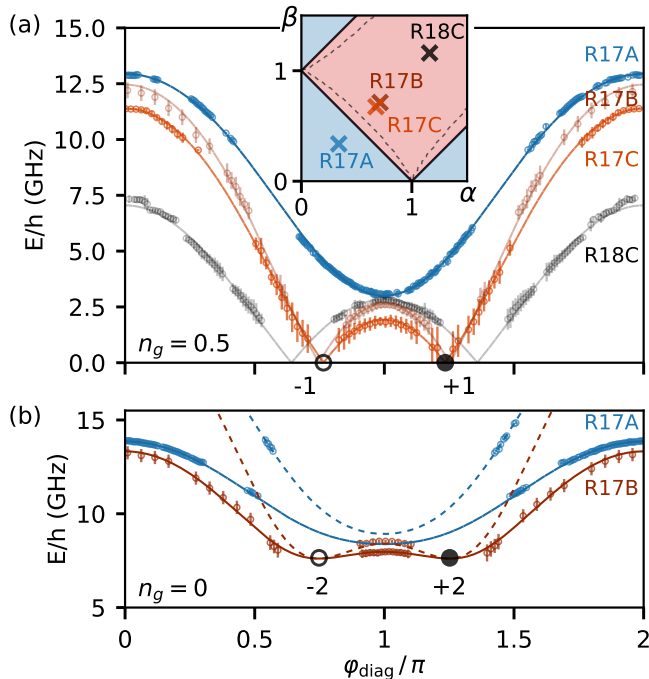


FIG. 5. BiSQUID transitions f_{01} (circles along solid lines) and f_{02} (circles along dashed lines) as a function of φ_{diag} extracted from two-tone spectroscopy measurements at $n_g = 1/2$ (a) and $n_g = 0$ (b) for different devices. Error bars indicate measured full-width half maximum of transitions, and lines are best fits to the data using the BiSQUID Hamiltonian. Inset shows phase diagram with placement of devices in topologically non-trivial (red) and trivial (blue) regions, separated by the critical line (solid), which is shifted (dashed) when taking into account geometric inductance, $\beta_L = 0.1$. Labels at degeneracies indicate the winding number N_2 .

VI. DISCUSSION

The Hamiltonian is obtained via standard circuit quantization [12] in a form incorporating the effective Josephson energy $E_J^*(\varphi_L, \varphi_R)$ [Eq. (2)],

$$H = E_C(n - n_g)^2 - (E_J^*e^{i\theta} + \bar{E}_J^*e^{-i\theta})/2, \quad (3)$$

and reduces to the charging Hamiltonian H_C when $E_J^* = 0$ (\bar{E}_J^* is the complex conjugate of E_J^*). Expanding out the flux dependence in E_J^* we have the more familiar form,

$$H = E_C(n - n_g)^2 - E_J \cos \theta - E_J \alpha \cos(\theta - \varphi_L) - E_J \beta \cos(\theta + \varphi_R). \quad (4)$$

	R17A	R17B	R17C	R18C	R16
f_r (GHz)	8.096	9.001	8.171	7.245	9.178
Q_L	37 520	4 200	65 460	17 520	5020
Q_{ext}	185 000	75 000	185 000	50 000	7400
E_J/h (GHz)	9.37	6.24	5.53	2.15	7.56
α	0.34	0.71	0.67	1.16	1.02
β	0.34	0.71	0.67	1.16	0
E_C/h (GHz)	7.93	7.61	8.34	16	9.05
$\omega_p/2\pi$ (GHz)	15.78	15.17	14.72	15	16.61
$E_{01,\text{min}}/h$ (GHz)	3.0	0	0	0	0.2

TABLE I. Summary of parameters of BiSQUID devices and control device SQUID R16 [Appendix G].

We fit the transitions measured as a function of φ_{diag} for $n_g = 1/2$ and $n_g = 0$ to the eigenenergies of the BiSQUID Hamiltonian Eq. (4) using three free parameters: E_C , E_J , and outer junction symmetry parameter $\alpha = \beta$. These fits are plotted as solid lines (f_{01}) and dashed lines (f_{02}) in Fig. 5, and show good agreement with the data (circles). Plots of the fit for f_{01} are also overlaid on the spectra Fig. 4(c,d) as dashed lines.

The circuit parameters obtained from fits, along with properties of the resonator, are given in Table I and are consistent with geometric estimates based on scanning electron microscopy. As a control, we also performed spectroscopy of a SQUID (device R16), which was designed to be symmetric, and fit to a model in which $\beta = 0$ [Appendix G]. Fitting yields a gap for the BiSQUID in the topologically trivial regime and the control SQUID. In the case of the SQUID the gap is due to a residual junction asymmetry of 2% resulting from variability in fabrication.

As in Fig. 4, the most indicative qualitative feature of a topologically non-trivial regime at $n_g = 1/2$ is the existence of negative curvature in f_{01} near $\varphi_{\text{diag}} = \pi$, as observed in samples R17B, R17C, and R18C [Fig. 5(a)]. This is in contrast to sample R17A (blue), which has a spectrum with positive curvature at $\varphi_{\text{diag}} = \pi$ reminiscent of an asymmetric SQUID. As shown in the phase diagram (inset), of the topologically non-trivial devices, sample R17C with $\alpha = \beta \approx 0.67$ is closest to the critical line $\beta = 1 - \alpha$. In this case the degeneracy triangle is more oblique, with angles $\varphi_{L,R}$ [Fig. 2] closer to π . Hence the region of negative curvature is smaller, more closely confined to a region around $\varphi_{\text{diag}} = \pi$.

The unbroken SUSY regime, $n_g = 0$, is shown in Fig. 5(b). Data of the topologically non-trivial device R17B (red) shows negative curvature at $\varphi_{\text{diag}} \approx \pi$ for both transitions f_{01} and f_{02} . This is in agreement with the model, plotted as a red solid line (f_{01}) and dashed line (f_{02}). The negative curvature in the topologically non-trivial state is in contrast to the expectation for device R17A, where the fit lines for f_{01} and f_{02} do not intersect and both transitions would have positive curvature near π . For this sample there is no data at $\varphi_{\text{diag}} \approx \pi$ because the resonator frequency is coincident with the transition frequency. In the unbroken SUSY state ($n_g = 0$), the lack

of data where f_{01} is degenerate with f_{02} at $\varphi_{\text{diag}} \approx 0.75\pi$ (indicated by ± 2 winding number), is due to the vanishing of the resonator frequency shift, similarly to what occurs for the ground state degeneracy in broken SUSY ($n_g = 1/2$) [60].

As with topological insulators, negative band curvature at a high-symmetry point can be indicative of an inverted gap. Indeed the phase diagram is described by a topological invariant which relates the curvature of the ground state band at high-symmetry points to the validity of the triangle inequality. At the four inequivalent high symmetry points $(\varphi_L, \varphi_R) = (0, 0), (0, \pi), (\pi, 0), (\pi, \pi)$ of the 2D Brillouin zone, there is time-reversal symmetry and $E_J^*(\varphi_L, \varphi_R)$ is real. As shown in Appendix B, the triangle inequality can be fulfilled only if one of the three points $[(0, \pi), (\pi, 0), (\pi, \pi)]$ has negative E_J^* . The \mathbb{Z}_2 curvature invariant B is defined as the product of the signs of E_J^* evaluated at these points. From the Hamiltonian Eq. (3), the sign of the expectation value of $\cos\theta$ in the ground state, $\text{sgn}\langle\cos\theta\rangle_0$, must be equal to the sign of E_J^* at each of the symmetry points in order to minimize the energy. Therefore B can also be calculated from the product of the signs of the ground state expectation values $\langle\cos\theta\rangle_0$ over the symmetry points.

Using the Hellmann-Feynman theorem, it can be shown that for $\alpha = \beta$, the curvature of an energy band in the φ_{diag} direction at $\varphi_{\text{diag}} = \varphi_L = \varphi_R = \pi$ is proportional to the expectation value of $\langle\cos\theta\rangle$ [Appendix B]. The sign of the curvature measured for the transition energy f_{01} at $\varphi_{\text{diag}} = \pi, n_g = 1/2$ is then related to $\text{sgn}\langle\cos\theta\rangle_0$. Furthermore, for the experimentally realized devices where $\alpha, \beta < 1$ (R17A, R17B, R17C), it suffices to determine the sign of $\langle\cos\theta\rangle_0$ at the unique point $\varphi_{\text{diag}} = \pi$ to determine B . Hence the sign of the curvature at $\varphi_{\text{diag}} = \pi$ of the measured spectra Fig. 5(a) is a direct indication of whether the device is topologically non-trivial.

In topological insulators with inversion and time-reversal symmetry, there is a similar \mathbb{Z}_2 invariant calculated from the product of parity eigenvalues over the high symmetry points [61]. For the BiSQUID, B is not a band invariant since it is only defined for the ground state, but it encodes information about the junction asymmetries and hence the triangle inequality.

In the topologically non-trivial regime one can also assign a topological charge to each degeneracy, or diabolical point, calculated from integrating the Berry curvature on a surface enclosing the degeneracy [3, 10, 49]. This local topological charge, or winding number N_2 [62], is distinct from the Witten index, which characterizes the global structure of the degeneracy “ladder” [Fig. 1], and the band inversion invariant which determines the global phase diagram [Fig. 2(e)]. In the broken SUSY configuration, Fig. 5(a), the topological charge of the ground state degeneracy is either $+1$ or -1 , as indicated by black circles. In unbroken SUSY (b), the topological charges of the degeneracies between states $|1\rangle$ and $|2\rangle$ are ± 2 , as in-

dicated by black circles. Higher order degeneracies have correspondingly higher charges, but are odd for $n_g = 1/2$ and even for $n_g = 0$ [23]. Along the critical line of the phase diagram separating trivial and non-trivial states, the degeneracies merge and the integral of the Berry curvature around the band intersection is zero, equal to the sum of the topological charges.

Higher experimental sensitivity would allow the measurement of transitions closer to the degeneracy points at $n_g = 0$ and $n_g = 1/2$. However spectroscopic techniques can only give an upper bound to a possible energy gap. Thermal effects, sample disorder, and instrument limitations set bounds on the emission linewidth and detector resolution, ultimately determining the smallest transition that can be measured. Controversy over the existence of a gap occurred previously in angular resolved photoemission studies of epitaxial graphene [63–65].

Despite the fact that the data is consistent with a Hamiltonian [Eq. (3)] which has a non-trivial phase, one cannot exclude that unknown, perturbative, terms open a gap in the region of the spectrum that we cannot resolve experimentally. Although many possible mechanisms could introduce such terms, including capacitive non-linearities [66], we only discuss the role of Josephson harmonics and the loop inductance.

Higher order Josephson effects are important in short, transparent superconducting weak links and add harmonic terms of the type $\cos k\theta$ for $k > 1$, corresponding to the simultaneous tunneling of multiple Cooper pairs. These processes, which are related to multiple Andreev reflections, are always weaker than the single Cooper pair tunneling process. Although they are strongly suppressed in typical tunnel junctions, they can occur when there are defects [67]. Increased junction transparency can be incorporated in the effective Josephson energy [Eq. (2)] by adding exponential terms with arguments $ik\varphi_{L,R}$ with $k > 1$. The triangle condition for degeneracy will be modified but can still be satisfied. Considering the symmetry point $\varphi_L = \varphi_R = \pi$, the even and odd harmonic terms in the effective Josephson energy will sum with opposite signs, in effect making it harder to “close” the triangle when even harmonics are present. However one can compensate by increasing the total Josephson energy of the outer junctions. The size of the non-trivial region of the phase diagram will therefore shrink as the junction transparency increases and higher order Josephson terms become more important, but will not disappear completely.

The superconducting loops of the BiSQUID will have a small inductance, both geometric and kinetic, which can be accounted for by adding terms of the form $E_L\gamma^2 = E_J/\beta_L\gamma^2$, where β_L is the ratio of the loop inductance to the Josephson inductance and γ the phase drop across the inductance. In the perturbative limit $\beta_L \ll 1$, inductances effectively reduce the Josephson energy of the junctions by a factor $\cos\rho\gamma \approx 1 - (\rho\gamma)^2/2$ where ρ is a coefficient of order unity depending on the geometry [Appendix C]. Replacing γ^2 by its expectation value for

an l -photon oscillator state, the renormalization factor is approximately $1 - \rho^2 \frac{2l+1}{4} \sqrt{E_C/E_L}$. Therefore when accounting for inductance, the low-lying degeneracies of a BiSQUID will not be lifted if the BiSQUID is deep in the topologically non-trivial regime, far from the critical lines. However for highly excited BiSQUID states, the oscillator degrees of freedom may be in a large number state $m \gg 1$ and it will be harder to satisfy the triangle inequality.

Solving numerically for the energy levels in the presence of arbitrary loop inductance [Appendix C], we find that although the lowest lying degeneracies persist, both for integer and half-integer n_g , higher order degeneracies may split according to their topological charge or even merge and open a gap [68]. The deformation of the phase diagram for the ground state degeneracy at $n_g = 1/2$ due to an artificially large series inductances $\beta_L = 0.1$ on each branch of a BiSQUID with $E_J = E_C = \sqrt{E_{JL}E_{CL}} = \sqrt{E_{JR}E_{CR}}$ is shown in the inset of Fig. 5(a). For small β_L , the prediction of the perturbative model for the shift in the phase diagram of the position of the critical line near the point $\alpha = \beta = 1/2$ agrees with numerical results [Appendix C]. Similarly to the effect of higher order Josephson terms, the inductive perturbation reduces the size of the topologically non-trivial region. However, whereas the phase diagram accounting for junction transparency is identical for all excited states, leading to a supersymmetric spectrum [Fig. 1] in the topologically non-trivial state, the inductive terms will gap out states at high enough energy. Accounting for inductance, supersymmetry is effectively destroyed in the ultra-violet limit. The role of additional bosonic degrees of freedom in lifting supersymmetry at the superconducting critical point of fermionic Dirac/Weyl systems has been considered previously [44].

VII. CONCLUSION

The BiSQUID is a model topological system which has at least three different topological invariants: the curvature invariant B , the Witten index $\text{Tr } P$, and the winding number N_2 . The curvature invariant, which is a function of the relative Josephson junction energies, determines whether a given BiSQUID sample can have degeneracies. For negative B , the structure of degeneracies is characterized by the Witten index, and the winding number classifies individual degeneracies. We have measured the curvature invariant directly via microwave spectroscopy of the ground state transition. The spectra are fit to a model with a supersymmetric degeneracy structure from which we infer the winding numbers of the degeneracies.

In future experiments, both the resonator-BiSQUID coupling and BiSQUID excitation should be modified to optimize the dispersive shifts near level crossings. It is also desirable to excite high-order level crossings, demonstrating that they occur at the same bias point, establishing the defining characteristic of SUSY. This requires

pumping transitions at higher frequencies, pumping with multiple drive tones, using alternative techniques such as amplitude spectroscopy [69], and optimizing the Josephson junction plasma frequency and resonator frequency. Single tone measurements with a low-frequency resonator should directly give the ground state band curvature and could be a powerful probe of circuit topological properties. Increasing the loop inductance β_L with granular aluminum [70] or other high-kinetic inductance materials may lead to the observation of gapping of high order degeneracies and the lifting of supersymmetry. With three-tone spectroscopy one may also be able to probe transitions from excited states, such as f_{12} .

By measuring the transition energies along multiple flux axes and determining the Gaussian curvature at $\varphi_{\text{diag}} = \pi$, it may be possible to obtain the topological invariant B for the general case $\alpha \neq \beta$. The numerically calculated energy bands [Fig. 4(c,d)] indicate a saddle point or negative Gaussian curvature for topologically non-trivial devices with $\alpha = \beta$, but this may be true in general. Other pump-probe spectroscopic techniques [71–73] should be able to directly determine the winding number of degeneracies.

We have shown how the topological properties are sensitive to realistic perturbations. Whereas the higher order Josephson effect does not affect supersymmetry, it is lifted at high energies by inductances. Neglect of the role of perturbations can lead to the misinterpretation of experimental results and tenuous claims of topological non-triviality [74, 75]. Further theoretical work should elucidate how the supersymmetric spectrum at $n_g = 0$ and $n_g = 1/2$ is modified as β_L is increased and predict the splitting and merging of high order topological charges.

Experiments on devices with an additional junction and one more loop, the TriSQUID, would effectively allow in-situ tuning of the junction asymmetry α [25, 76]. One could then traverse the phase diagram, switching between topologically trivial and non-trivial regimes, with an additional local flux line. Crossing the critical line would allow observing the merging of Weyl points and the opening of a gap [77]. With more sophisticated circuits, one could perform Weyl point teleportation [78] or probe higher order topological invariants [79].

It would also be interesting to investigate, both theoretically and experimentally, the existence of supersymmetry in circuits with many junctions [80] or circuits with non-tunnel junctions, which harbor Andreev states [81]. Single [82–85] or multi-terminal [26, 86, 87] circuits with Andreev states may have degeneracies described by supersymmetry [88].

With respect to topological order in condensed matter systems, the material analog of a BiSQUID is 2D spinless graphene. It remains to establish a general mapping between the topological classes of materials [9, 89, 90] and Josephson junction based circuits. Inversion symmetry plays an important role in the BiSQUID and it may be possible to establish the link between the

“weak” BiSQUID invariants, $\text{sgn} \langle \cos \theta \rangle$ at high symmetry points, the “strong” invariant B , and the corresponding topological invariants of inversion symmetric fermionic topological insulators [61]. Sub-lattice symmetries [Appendix A] can also lead to degeneracies, as in Weyl semimetals and Josephson junction circuits with higher order terms [91]. Although one can define a Brillouin zone for the BiSQUID, it does not have a boundary in real space and therefore no edge states. On the other hand, it is possible to use Josephson junctions to produce high-dimensional topological systems without any real-world analog [25]. A full classification of the topological properties of arbitrary Josephson junction circuits is lacking [14, 76].

The dual circuit of the BiSQUID, the Cooper pair pump, and its variants have been in development for current metrology [92]. In addition several proposals exist for transconductance quantization exploiting topological properties of Josephson tunnel junction circuits [24, 93]. Similar spectroscopic techniques as employed here for BiSQUIDs could help evaluate the suitability of the proposed circuits for metrology applications. Circuits similar to the BiSQUID can also serve for quantum information, where its topological properties can help mitigate decoherence or decay [8, 94–98], or offer platforms for geometric and holonomic computation [99–101].

Appendix A: Supersymmetry of Charging Hamiltonian

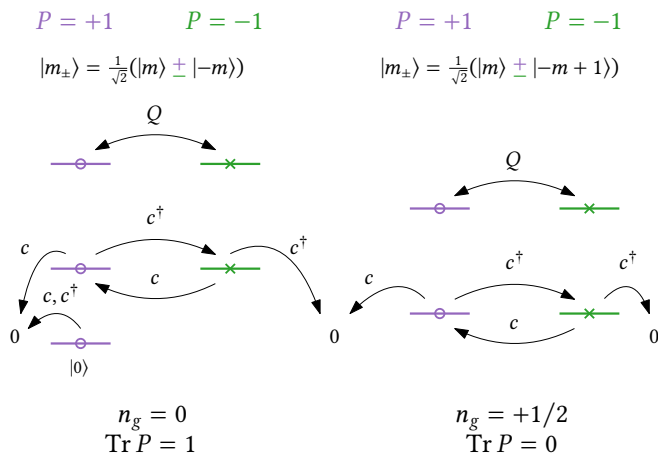


FIG. 6. Quantum mechanical supersymmetry of charging Hamiltonian. Supercharge operator Q exchanges eigenstates of even parity $|m_{+}\rangle$ (bosonic) and odd parity $|m_{-}\rangle$ (fermionic) for $m_{\pm} > 0$. The fermion number operator $c^{\dagger}c$ annihilates bosonic states while leaving fermionic states invariant. Eigenstates are written in charge basis $|m\rangle$ satisfying $Q|m\rangle = \sqrt{E_C}(m - n_g)|m\rangle$.

Fig. 6 is a diagram of the quantum mechanical supersymmetry properties of the charging Hamiltonian H_C at $n_g = 0$ and $n_g = +1/2$. The simultaneous parity

and energy eigenstates are given by $|m_{\pm}\rangle = \frac{1}{\sqrt{2}}(|m\rangle \pm |-m + 2n_g\rangle)$ where $m > 0$, except for the unique ground state at $n_g = 0$ which is given by $|0\rangle$. Note that charge eigenstates $|\pm m\rangle$ are distinct from energy eigenstates $|m_{\pm}\rangle$. For unbroken SUSY, $n_g = 0$, the real wavefunctions are sines and cosines with wavevector m , whereas for broken SUSY, $n_g = 1/2$, the complex wavefunctions have a magnitude given by sines and cosines with wavevector $m/2$.

For $n_g = 0$ and $n_g = +1/2$ we therefore have $P|m_{\pm}\rangle = \pm|m_{\pm}\rangle$ and $H_C|m_{\pm}\rangle = E_m|m_{\pm}\rangle$ with $E_m = E_C(m - n_g)^2$. The positive sign corresponds to even parity, or “bosonic” states, and the negative sign to odd parity, or “fermionic” states.

The supersymmetry operator $Q = \sqrt{E_C}(n - n_g)$ swaps parity, or exchanges the bosonic and fermionic states, up to a multiplicative factor, $Q|m_{\pm}\rangle = \sqrt{E_C}(m - n_g)|m_{\mp}\rangle$. By construction we obtain the fundamental spectral property of supersymmetry: for an eigenstate $|m_{\pm}\rangle$ with non-zero energy, $Q|m_{\pm}\rangle$ is a *distinct* degenerate eigenstate. The uniqueness of the two states ultimately arises from the anti-commutator $\{P, Q\} = 0$ (Eq. (1)). When a symmetry operator S commutes with the Hamiltonian, unless the operator is anti-unitary, the eigenstates $|\psi\rangle$ and $S|\psi\rangle$ may be equivalent up to a phase factor. But since both P and Q commute with the Hamiltonian and the anti-commutator $\{P, Q\}$ is zero, one can show that for any non-zero energy eigenstate $|\psi\rangle$, either $P|\psi\rangle$ or $Q|\psi\rangle$ is also an eigenstate and differs from $|\psi\rangle$.

For the bosonic charging Hamiltonian, the supersymmetry is hidden, in the sense that there is no explicit fermionic degree of freedom. However we can identify a “fermionic” operator $c = \frac{1+P}{2}Q$, which swaps parity and then projects states to the even, or bosonic sector. Since $\{P, Q\} = 0$, the adjoint $c^{\dagger} = \frac{1-P}{2}Q$ also swaps parity but projects to the odd sector. The operators c, c^{\dagger} are “fermionic” in the sense that they satisfy $c^2 = c^{\dagger 2} = 0$ and $\{c, c^{\dagger}\}/E_m = 1$ for all eigenstates with non-zero energy. When applied to a “fermionic” state $|m_{-}\rangle$, the fermionic number operator $c^{\dagger}c$ is the identity (up to a constant), but $c^{\dagger}c$ annihilates a “bosonic” state $|m_{+}\rangle$, hence the particle naming convention for the different parities.

Using the fermion number operator or parity operator, one can partition the Hilbert space in two, and rewrite the Hamiltonian in terms of Pauli matrices [47]. This process yields a supersymmetric Hamiltonian in the same way that in conventional SUSY QM, a Hamiltonian with a generic potential but no explicit fermionic component is supplemented by its superpartner [37, 38].

A normalized analogue to the superexchange operator can be defined as $q = Q/\sqrt{H_C} = (n - n_g)/|n - n_g| = \text{sgn}(n - n_g)$ which is unitary if we take the convention $\text{sgn}(0) = +1$ and not 0. Like P , q is a grading operator which squares to the identity and partitions states by the sign of the charge relative to n_g . Note that with unitary q , since $q|0\rangle = |0\rangle$, the fundamental SUSY anti-commutator $\{q, P\}$ is zero for all eigenstates except the ground state at $n_g = 0$. For $n_g = 1/2$, since the eigen-

states $|m_{\pm}\rangle$ mix even and odd charge states, the superexchange operator can also be written $q = e^{i\pi n}$, which in the position basis is a half-lattice translation.

Degeneracies in the spectrum can also be understood as arising from Kramers theorem. The anti-unitary symmetry PqK , where K is time reversal (complex conjugation in the charge basis), squares to negative one for all eigenstates except the ground state at $n_g = 0$. Therefore all non-zero energy eigenstates are Kramers pairs. This statement is equivalent to the SUSY degeneracy theorem. At $n_g = 1/2$, Pq can be considered a glide symmetry, since P is a reflection and $q = e^{i\pi n}$ is a half-lattice translation. Such sub-lattice symmetry also arises in Weyl/Dirac systems [102].

For the five-junction unbroken supersymmetric circuit proposed by Ulrich et al. [46], the grading operator is the same as for $n_g = 0$, but the supercharge has an additional “non-trivial” term proportional to $\sin\theta$. At a special value of the proportionality constant, all states except the ground state are doubly degenerate. Unfortunately the supersymmetry is not robust to imperfections in the fabrication process and the circuit is more difficult to realize experimentally.

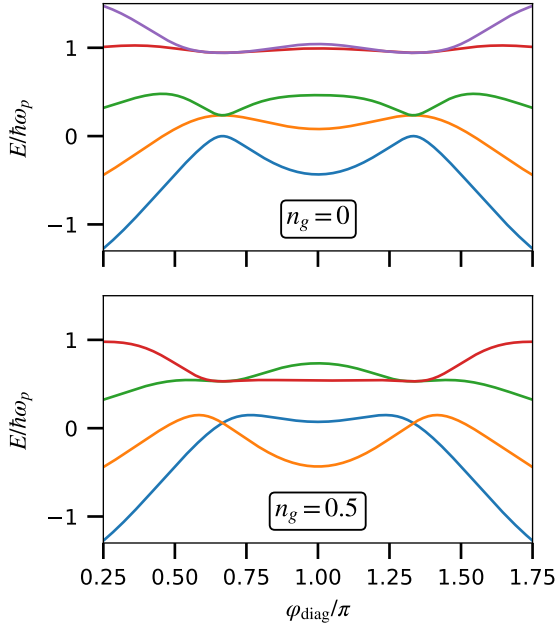


FIG. 7. Plot of the first few energy levels of a fully symmetric topologically non-trivial BiSQUID with $E_C = E_J/3$ and $\alpha = \beta = 1$. When $\varphi_{\text{diag}} = \pm 2\pi/3 \approx \pm 0.67\pi$, the triangle condition is satisfied and the effective Josephson energy E_J^* is zero. In the unbroken SUSY case ($n_g = 0$, top) all states except the ground state at zero energy are doubly degenerate. For broken SUSY ($n_g = 1/2$, bottom), all states are doubly degenerate. Line colors determined by wavefunction continuity [103].

φ_L, φ_R	E_J^*	$\text{sgn } E_J^*$		
		$1 \leq \beta \leq \alpha$	$\beta < 1 \leq \alpha$	$\beta \leq \alpha < 1$
$(0, 0)$	$1 + \alpha + \beta$	+	+	+
$(\pi, 0)$	$1 - \alpha + \beta$	\pm	\pm	+
$(0, \pi)$	$1 + \alpha - \beta$	+	+	+
(π, π)	$1 - \alpha - \beta$	-	-	\mp
$\prod \text{sgn } E_J^*$		\mp	\mp	\mp

TABLE II. Calculation of curvature invariant B .

Appendix B: Curvature Invariant

We show that the curvature invariant B , the product of $\text{sgn } E_J^*$ over the high symmetry points, encodes the triangle condition in Fig. 2 by enumerating its value for all possible configurations of α, β [Table II]. At the four high symmetry points $(\varphi_L, \varphi_R) = (p\pi, q\pi)$ where $p, q = 0$ or 1 (first column), the effective normalized Josephson energy $E_J^*(\varphi_L, \varphi_R)$ Eq. (2) can be written $1 + (-1)^p\alpha + (-1)^q\beta$ (second column). Assuming that $\alpha \geq \beta$ without loss of generality, there are three possible orderings of the Josephson energies relative to E_J : $1 \leq \beta \leq \alpha$, $\beta < 1 \leq \alpha$, and $\beta \leq \alpha < 1$ (top row). Except for the last row, the cells with $+, -, \pm, \mp$ gives the sign of E_J^* for the corresponding high symmetry point and Josephson energy ordering. For the cells with two possibilities, the sign of E_J^* needs to be resolved by using the triangle inequality: whether the sum of the smallest of $1, \alpha, \beta$ is greater than the largest one. For the orderings in columns three and four, the triangle inequality is $1 + \beta \geq \alpha$ and for the last column, it is $\alpha + \beta \geq 1$. For the double entries indicated by \pm or \mp , the top sign corresponds to the Josephson energy configuration that satisfies the triangle inequality.

The last row gives the product of the signs along a column, which is equivalent to the topological curvature invariant B . In all columns, the product is negative if and only if the upper sign in \pm or \mp is taken, or equivalently when the triangle inequality is satisfied. Therefore, independent of the Josephson energy ordering, $B = -1$ implies that the triangle inequality can be satisfied.

To relate B to the curvature E_j'' of the j -th energy band along the direction φ_{diag} for the mirror symmetric configuration $\alpha = \beta$, we first rewrite the potential energy term in the Hamiltonian Eq. (4) as a function of flux variables $\sigma = (\varphi_R + \varphi_L)/2$ and $\delta = (\varphi_R - \varphi_L)/2$, $-E_J(1 + 2\alpha \cos\sigma \cos(\theta + \delta))$. With this transformation, the diagonal $\varphi_{\text{diag}} = \varphi_R = \varphi_L$ in the Brillouin zone Fig. 4(a) is equivalent to $\sigma = \varphi_{\text{diag}}, \delta = 0$. Therefore the prime notation $'$ refers to derivatives with respect to σ .

Taking the derivative of the Hellmann-Feynman theorem $E_j' = \langle \psi_j | H' | \psi_j \rangle$, where $|\psi_j\rangle$ is the j -th energy eigenstate, we obtain an expression for the curvature,

$$E_j'' = \langle \psi_j | H'' | \psi_j \rangle + \langle \psi_j' | H' | \psi_j \rangle + \langle \psi_j | H' | \psi_j' \rangle.$$

At the high symmetry point $\varphi_{\text{diag}} = \pi$, or $\sigma = \pi, \delta = 0$, the last two terms are zero as long as $\alpha = \beta$. Hence

$E_j''/E_J = -2\alpha \langle \cos \theta \rangle_j$ and the curvature is proportional to $\langle \cos \theta \rangle_j$, the expectation value of $\cos \theta$ in state $|\psi_j\rangle$.

All measured devices except R18C have Josephson energies satisfying the inequality $\alpha \approx \beta < 1$. According to the last column of the table above, for $\alpha, \beta < 1$ the invariant B will be given by the sign of the effective Josephson energy at $\varphi_{\text{diag}} = \pi$ (last row), or equivalently the sign of $\langle \cos \theta \rangle$ in the ground state, $\langle \cos \theta \rangle_0$. From the numerical surface plots of the first two energy manifolds, insets Fig. 4(c,d), one sees that E_0'' is expected to be positive for the topologically non-trivial configuration ($B = -1$) and negative in the trivial configuration ($B = 1$). This concurs with $\text{sgn} E_0'' = -\text{sgn} \langle \cos \theta \rangle_0 = -B$ as inferred from the formula $E_j''/E_J = -2\alpha \langle \cos \theta \rangle_j$.

Since Fig. 5 shows the transition energy f_{01} , the curvature of the data at $\varphi_{\text{diag}} = \pi$ should be compared to $E_1'' - E_0'' = -2\alpha E_J (\langle \cos \theta \rangle_1 - \langle \cos \theta \rangle_0)$. At $\varphi_{\text{diag}} = \pi$ and for $n_g = 0$ or $n_g = 1/2$, the parity operator P commutes with the Hamiltonian and energy eigenstates are also parity eigenstates. Wavefunctions constructed from the $n_g = 1/2$ parity basis, $|m\pm\rangle = 1/\sqrt{2}(|-m\rangle \pm |m+1\rangle)$ [Appendix A], always have a node at either $\theta = \pi$ (positive parity) or $\theta = 0$ (negative parity). Therefore the expectation value $\langle \cos \theta \rangle_1$ of the first excited state, which has opposite parity than the ground state, cannot be larger in absolute value than $\langle \cos \theta \rangle_0$. This implies that $\text{sgn}(E_1'' - E_0'') = -\text{sgn}(\langle \cos \theta \rangle_1 - \langle \cos \theta \rangle_0) = \text{sgn} \langle \cos \theta \rangle_0 = B$.

As stated in the main text, the sign of the curvature measured at the high symmetry point $\varphi_{\text{diag}} = \pi, n_g = 1/2$ is a direct indication of B for all samples except R18C, which has $\alpha \approx \beta > 1$. For R18C, looking at [Table II], the curvature is always negative at $\varphi_{\text{diag}} = \pi$ and a second measurement of the curvature at $\varphi_L = \pi, \varphi_R = 0$ would be needed to resolve the triangle inequality. However, in practice since we know that $\alpha \approx \beta \approx 1.16$ for R18C [Table I], we expect the triangle inequality $1 + \beta \geq \alpha$ to be satisfied and that a measurement of the curvature at $\varphi_L = \pi, \varphi_R = 0$ would have positive sign. The blue curve in Fig. 5(a) ($n_g = 1/2$) for the gapped device R17A has positive curvature ($B = 1$) at $\varphi_{\text{diag}} = \pi$ whereas the two gapped devices (red) have negative curvature ($B = -1$).

Appendix C: Role of Inductance

The BiSQUID Hamiltonian Eq. (4) can be modified to incorporate inductances on each branch,

$$H_l = H_1(n_1, \theta_1) + H_2(n_2, \theta_2) + E_{C\Sigma}(n - n_g)^2 + \\ -E_J[\cos(\theta + \gamma_1\theta_1 + \gamma_2\theta_2) + \\ \alpha \cos(\theta + \gamma_3\theta_1 + \gamma_4\theta_2 - \varphi_L) + \\ \beta \cos(\theta + \gamma_5\theta_1 + \gamma_6\theta_2 + \varphi_R)],$$

where $H_i(n_i, \theta_i)$ are harmonic oscillator Hamiltonians describing the two normal modes of the linear part of the circuit composed of branch capacitors and inductors.

The coordinates of the normal modes are the conjugate quantum variables n_i, θ_i . Each mode has frequency ω_i and dimensionless impedance z_i which is the characteristic impedance scaled by a resistance $\hbar/(2e)^2$. The constants $\gamma_i < 1$ are participation ratios [104] and describe the coupling of the harmonic modes to the Josephson junction phases. The effective Josephson degrees of freedom n, θ are associated to a common mode with charging energy $E_{C\Sigma} = (2e)^2/(C_J + C_L + C_R)$ where $C_{L,R}$ are the capacitances on the left and right branch.

When the Josephson energies are smaller than the inductive energies one can neglect the last term in H_l and the eigenstates of the normal modes are harmonic oscillator number states $|l_1, l_2\rangle$. In this perturbative limit, $\beta_L \lesssim 1$ and $\alpha, \beta \lesssim 1/\beta_L$, we can trace out the oscillator degrees of freedom. Integrating H_l over the harmonic oscillator wavefunctions, the effective BiSQUID Hamiltonian in the presence of inductance is

$$H_l \approx \hbar\omega_1(l_1 + 1/2) + \hbar\omega_2(l_2 + 1/2) + E_{C\Sigma}(n - n_g)^2 + \\ -E_J[\rho_0 \cos \theta + \alpha\rho_L \cos(\theta - \varphi_L) + \beta\rho_R \cos(\theta + \varphi_R)].$$

The Josephson energies of the junctions are renormalized by exponential factors

$$\rho_0 = e^{-\gamma_1^2(2l_1+1)z_1/4 - \gamma_2^2(2l_2+1)z_2/4} \\ \rho_L = e^{-\gamma_3^2(2l_1+1)z_1/4 - \gamma_4^2(2l_2+1)z_2/4} \\ \rho_R = e^{-\gamma_5^2(2l_1+1)z_1/4 - \gamma_6^2(2l_2+1)z_2/4}.$$

They depend not only on the participation ratios and impedances of the harmonic modes, but also on the photon occupation, resulting in a smaller topologically non-trivial phase as l_1, l_2 are increased.

We can now solve for the Josephson degrees of freedom n, θ with the only difference being the renormalization of the Josephson energies. The triangle inequality $|\alpha\rho_L - \beta\rho_R| < \rho_0 < \alpha\rho_L + \beta\rho_R$ can still be satisfied but the position of the critical lines in the phase diagram will be shifted. Since $\varphi_{L,R}$ is either 0 or π on the critical lines, one can solve the transcendental equations $\rho_0 \pm \alpha\rho_L \pm \beta\rho_R = 0$ to determine their positions. The solutions of these equations for the ground state $l_1 = l_2 = 0$ and $\beta_L = 0.1, 1$ (solid lines) shows excellent agreement with numerically obtained critical lines in the region $\alpha, \beta \lesssim 1/\beta_L$ [Fig. 8]. We use the python package scQubits [105, 106] to numerically diagonalize the BiSQUID Hamiltonian with inductance, determining the boundary between topologically trivial and non-trivial regions (circle markers) by computing the energy gap f_{01} for $n_g = 1/2$.

Appendix D: Fabrication

The devices are fabricated on 350 μm thick wafers of high-resistivity intrinsic silicon capped with a 150 nm SiO₂ surface oxide. We begin by cleaning the substrate

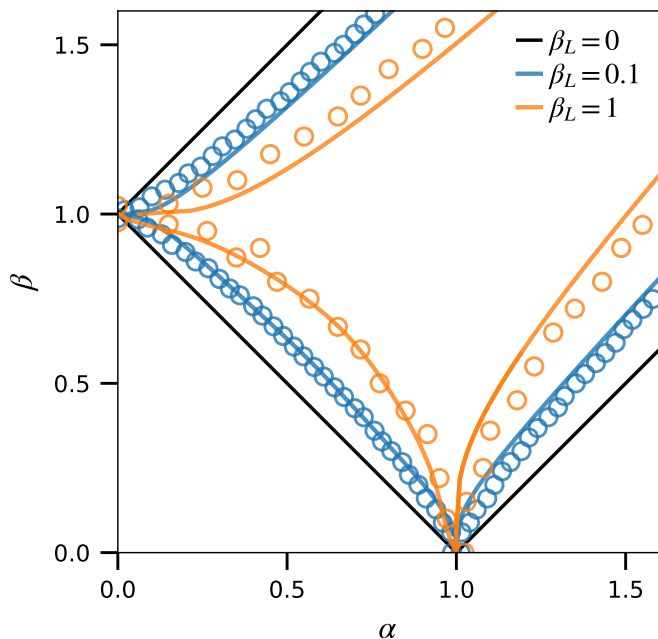


FIG. 8. BiSQUID phase diagram in the presence of inductance E_J/β_L on each branch. The critical line separating the topologically trivial and non-trivial phases is shown for $\beta_L = 0$ (zero inductance, black), $\beta_L = 0.1$ (blue) and $\beta_L = 1$ (orange). The solid lines for $\beta_L > 0$ are determined from the perturbative model [Appendix C]. The circle markers are obtained by numerical diagonalization of the BiSQUID Hamiltonian including inductance. The plasma frequency of each junction is kept constant for all α and β . The capacitance of the middle junction is fixed to $C_J = (8e^2 L_J)/(\varphi_0^2)$ with L_J the Josephson inductance of the middle junction and $\varphi_0 = \hbar/2e$ the reduced flux quantum.

using a soft oxygen plasma etching step in a reactive ion etcher. Next, we deposit a layer of aluminum on the entire wafer. This aluminum is deposited at a rate of 1 nm/s using a high-vacuum Plassys electron gun evaporator. Before exposing the wafer to ambient atmosphere, the aluminum is passivated in the Plassys in 200 mbar of pure dioxygen during 10 minutes.

In a first optical lithography step, we define the resonator, control lines, and alignment structures. To make the negative mask, we spin coat a layer of S1813 resist, bake it at 115°C for one minute, expose it using a LW405B laser writer with a dose of about 200 mJ/cm², and develop it in MF319 developer for one minute. To remove the aluminum in exposed areas, we perform a wet etch. This involves first hard baking the resist at 150°C for 3 minutes, followed by immersing the wafer in MF319 for 5 to 7 minutes and rinsing it with water. Then we dice the wafer in individual 10x10 mm² dies.

We then fabricate BiSQUID's Josephson junctions and test structures using electron-beam lithography. We spin coat a bilayer of MMA EL11 and PMMA 950 A4 at 3000 rpm for 60 seconds each. The lithography mask is patterned using a 30 kV FEI Magellan scanning electron

microscope equipped with Raith ELPHY quantum software. The typical Josephson junction area is 200x200 nm² with a critical current density of 150-200 nA μm⁻². The mask is developed in a 1:3 MIBK/IPA mixture for 55 seconds and rinsed in IPA for 60 seconds. The Josephson junctions are deposited using a Plassys electron-beam evaporator and a double-angle Dolan evaporation technique. Residual resist is removed by a soft oxygen plasma etch. Then a first layer of 12 nm of aluminum is deposited at a rate of 0.1 nm/s and an angle of 30°. The tunnel barrier is formed by exposing the junctions to 200 mbar of pure dioxygen for 10 minutes. A second layer of 80 nm of aluminum is deposited at a rate of 1 nm/s and an angle of -30°. The difference in thickness between the first and second electrodes leads to a superconducting gap difference across the junctions, which can prevent quasiparticles from tunneling across the junction [Appendix F]. The junctions are finally passivated in 200 mbar of pure dioxygen for 10 minutes. The resist is stripped using NMP 1165 for a few hours at 80°C.

The BiSQUID leads are capacitively coupled to the ground plane over an area of approximately 800 μm². We do not remove the aluminum oxide of the ground plane, so the connection is capacitive with a high capacitance. However for some devices (SQUID *R16* and BiSQUID *R17C*), an extra step has been added to connect test JJs to measurement pads. We use the same resist as for the first lithography and open small patching areas around test JJs leads and measurement pads. The resist is then hard-baked at 150°C for 3 minutes. In a Plassys electron-beam evaporator, we mill the aluminum oxide in two 4-minute argon milling steps with an acceleration voltage of 500 V and a current of 30 mA. We then deposit 100 nm of aluminum at a rate of 1 nm/s and passivate the aluminum by 10 min oxidation in 200 mbar of pure dioxygen.

Appendix E: Experimental setup

The simplified wiring used to perform two-tone spectroscopy is shown in Fig. 9. A vector network analyzer (VNA) is used to generate a signal at a frequency f_1 to probe the resonator. This signal is combined at the mixing chamber in a bias tee with a DC gate voltage V_g generated by a Yokogawa 7651 voltage source. The DC gate voltage is filtered by custom-made flexible cables with both lumped and distributed filtering, resulting in a low-pass cutoff of around 50 Hz and a voltage attenuation factor of 17. A second tone at a frequency f_2 is produced by an Agilent signal generator and combined with the DC current I_X in a second bias tee which is connected to the flux line. We use NbTi twisted pairs for the DC currents, with attenuation at the 4K stage and additional low-pass filtering at the mixing chamber stage. Microwave input signals are attenuated at different stages of the cryostat, with a total of around -75 dB for the f_1 line and -55 dB for the f_2 line. Low-pass and

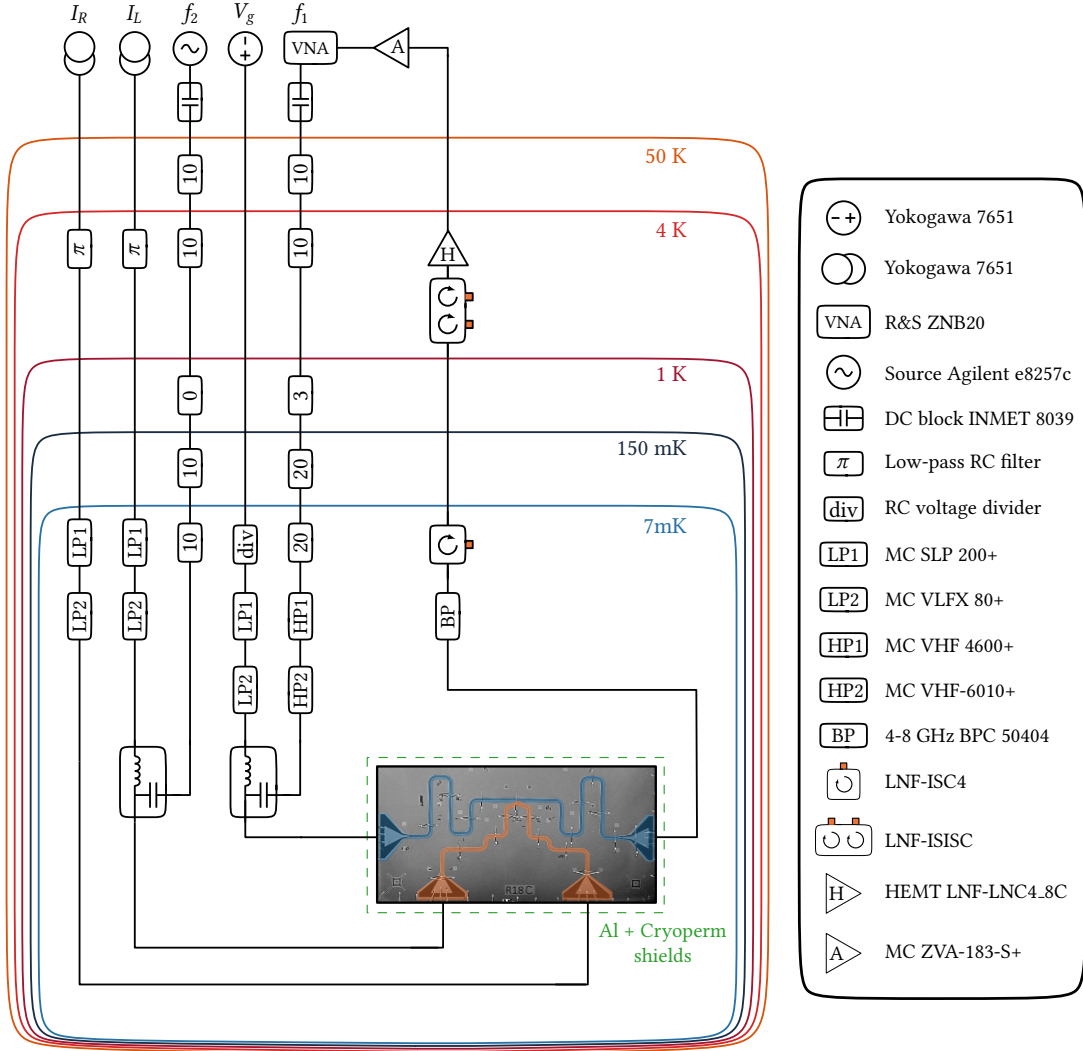


FIG. 9. Full wiring of the cryostat for two-tone spectroscopy experiments. NbTi twisted pair wires are used for DC currents I_L and I_R . An in-house flexible polyimide cable is used for the gate voltage V_g . It supports both distributed and lumped low-pass RC filtering at all stages of the fridge.

high-pass microwave filters are used on the DC and microwave lines respectively. Later in the experiment, we also added eccosorb filters on all DC and RF lines at the mixing chamber stage. However, we observe no significant change, and quasiparticle poisoning rates were unaffected by this additional filtering.

The output signal is amplified first at 4K with a LNF cryo-HEMT with a gain of 42 dB and again at room temperature with a Mini-Circuits ZVA amplifier with a gain of 26 dB. A Josephson traveling-wave parametric amplifier was also used for some measurements [107]. The BiSQUID device is isolated from amplifier noise by a Microtronics band-pass filter, a single isolator at the mixing chamber and a double circulator at 4K. The output signal is recombined with the reference signal in the VNA, enabling the transmission parameter S_{21} to be measured.

The measured resonator and BiSQUID parameters are given in Table I. To characterize the resonators, we fit

the transmission data to extract the loaded quality factor Q_L . We use the FastCap tool in LayoutEditor to estimate the external coupling capacitances from the CPW resonator to the feedlines. From these capacitances, we estimate the external quality factor Q_{ext} . The output capacitance is designed to be larger than the input capacitance such that most of the photons from the resonator are emitted into the output feedline. The CPW resonator is designed to have an impedance of 75 Ohm to increase its coupling with BiSQUIDs. The coupling of a BiSQUID and CPW resonator is estimated from vacuum Rabi splitting measurements. We find typical values of $g = 2\pi 20$ MHz. Further details are given in [76].

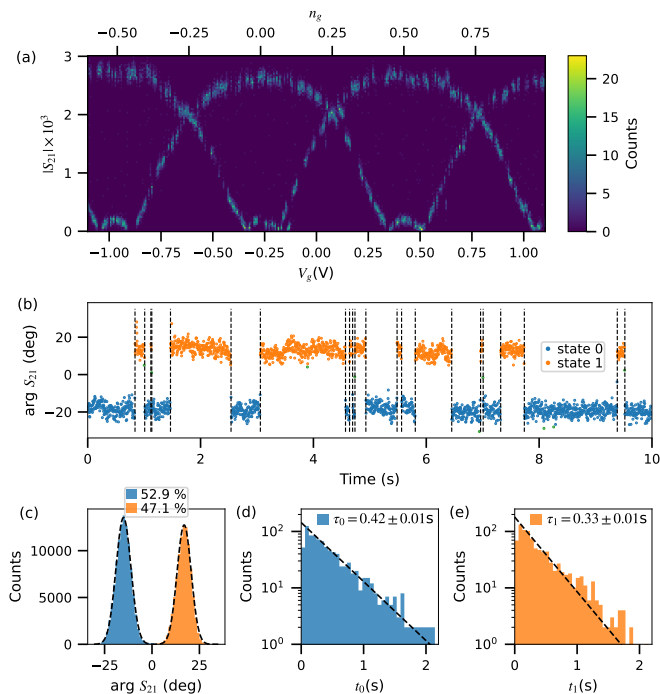


FIG. 10. Quasiparticle poisoning in BiSQUID R18. (a) Measured magnitude of the resonator transmission at fixed frequency as a function of gate voltage V_g for fixed $\varphi_L = \varphi_R = 0$. For each value of V_g , we collect 50 data points with an individual averaging time of 5 ms and indicate counts with the color scale. The two roughly sinusoidal lines shifted by approximately 0.68 V correspond to the two QP parities. Values of V_g are given after attenuation in the measurement lines. (b) First 10 seconds of an 800-second measurement of the resonator with an averaging time of 5 ms per point. The reduced flux threading the SQUID is set to $\varphi_{\text{diag}} \approx \pi$ and the charge offset to $n_g \approx 0.5$. Data points are separated in two parity states (blue, orange), then parity switching events are identified (black dashed lines). Outlier data (green markers) are not included in the analysis. (c) The histogram of the phase of the full time trace is fitted to two Gaussian peaks. We find two states with occupation probabilities of 53% for state 0 (blue) and 47% for state 1 (orange). (d, e) The histograms of occupation times t_0 of state 0 (d) and t_1 of state 1 (e) are fitted to exponential distributions with time constants τ_0 and τ_1 . The vertical axes indicate counts in logarithmic scale.

Appendix F: Quasiparticle poisoning

The presence of quasiparticles (QPs), or unpaired electrons, is harmful to many superconducting devices [54, 108]. The origin of these non-equilibrium QPs is still unclear, but possible explanations include stray infrared photons and ionizing radiation from environmental radioactive sources and cosmic rays [55, 57, 58, 109].

In the absence of QPs, the energy of a Josephson junction is periodic with the charge offset $2en_g$. However the tunneling of a QP through the junction changes the parity of the superconducting island and shifts the charge offset by $1e$. If QPs are tunneling to the island faster

than they recombine or tunnel out, the parity of the island will be constantly changing. By measuring faster than the parity switching time, we can observe the typical "eye-pattern" consisting of two states with different quasiparticle parity and $1e$ charge offset periodicity [Fig. 10(a)].

To extract the typical QP parity switching time, we measure the state of BiSQUID device R18 at $\varphi_{\text{diag}} \approx \pi$ and $n_g = 0.5$ during 800 seconds. The first 10 seconds of the time trace are shown in Fig. 10(b). We identify a parity switching event if the state of the system changes for at least three data points. From the histogram of the full time trace, we can clearly identify two states with similar average occupation of 50% [Fig. 10(c)]. We then extract all the occupation times t_i of state i and fit their histogram to an exponential distribution $f(t_i) = A \exp(-t_i/\tau_i)$ which yields time constants of about 0.4 s. We measure QP switching times at other values of φ_L, φ_R and n_g and found consistent switching times between 0.1 and 1 seconds.

We increased the superconducting gap Δ of the BiSQUID island by reducing the thickness of the aluminum to 12 nm, leading to an increase of about 40 μeV of Δ compared to the 80 nm thick aluminum layer used for the rest of the BiSQUID [Fig. 11]. This creates an energy barrier, potentially preventing QP from tunneling to the island [110–115]. Gap-engineering worked well in some devices, with typical QP tunneling time of several seconds and average population of poisoned parity of only few percents. However, the effectiveness of gap-engineering seems to be highly fabrication dependent and in most cases did not function properly. One possible explanation of the failure of gap-engineering is the presence of defects in the oxide barrier of the junctions which may form spatially localized subgap states [116]. We tried adding eccosorb filters to all DC and RF lines but did not observe any impact on QP poisoning. Increasing the attenuation of eccosorb filtering and improving the sample shielding with tight indium seals may help suppress the high-frequency photon flux and reduce quasiparticle poisoning [59].

In addition to quasiparticle parity switching, BiSQUIDs are also sensitive to charge noise which may be attributed to fluctuating two-level systems in dielectrics or surface defects [117]. By monitoring the charge offset over time, we observe random amplitude jumps approximately every ten minutes. We also observe a slow drift of the charge offset of order of 0.1% of a $2e$ period per minute [76]. To maintain a constant value of charge offset over a long measurement, we regularly perform quick calibration measurements. We probe the resonator while sweeping the charge offset of the BiSQUID over 1.5 periods. We set the reduced fluxes φ_L, φ_R of the BiSQUID such that its energy is close to the resonator without crossing it. This allows an easier fitting procedure to extract the correspondence between V_g and n_g . This calibration measurement takes about 5 seconds and we perform it every 1-2 minutes

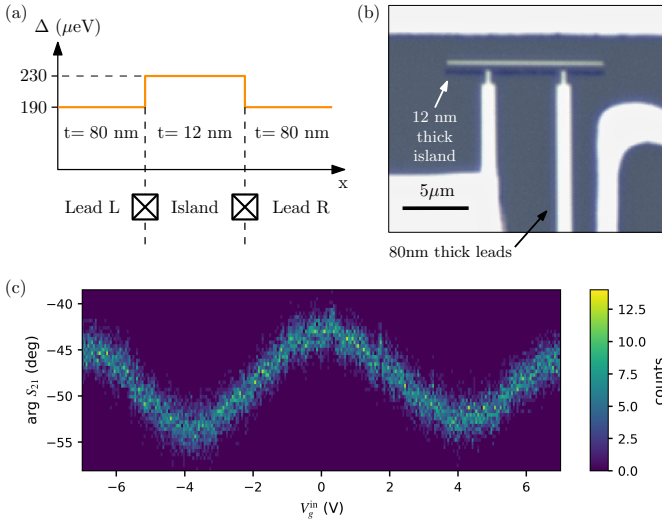


FIG. 11. Superconducting gap engineering using varying aluminum thicknesses. (a) The 12 nm thick island has a larger superconducting gap than the rest of the circuit. The extra energy of $\delta\Delta = 40 \mu\text{eV}$ can partially prevent QP from entering the island. (b) Optical microscope image of a SQUID with a 12 nm thick island (faint dark blue) and 80 nm thick leads (white). The thin island can only be seen with a large brightness. The mirror image of the island (white) is due to the angle evaporation technique, but is not connected to the rest of the circuit. (c) Resonator transmission measured as in Fig. 10 (a) but with the gap-engineered SQUID *R16*. Only a single quasiparticle state is observed, meaning that QP poisoning events are strongly suppressed. However, for several other fabrications of gap-engineered SQUIDs and BiSQUIDs with similar recipes and designs, the gap-engineering technique did not work and we observed typical QP parity switching times τ_i of 0.1-0.5 s.

to keep track of the charge offset. If we detect a small drift during a measurement, we adjust the charge offset accordingly, and if we detect a jump we discard the last data and measure it again.

Appendix G: SQUID data

We also performed the spectroscopy of a SQUID as a control experiment. Two external parameters control a SQUID energy levels: one reduced flux φ_X and one charge offset n_g . At half-flux quantum $\varphi_X = \pi$, a perfectly symmetric SQUID reduces to the charging Hamiltonian H_C which has a hidden quantum mechanical supersymmetry [Fig. 1]. However any asymmetry between left and right junctions prevents the cancellation of the effective Josephson energy E_J^* which lifts all the degeneracies of the energy levels.

The SQUID circuit *R16* was designed to be symmetric with equal Josephson energies, however the fabrication process introduces a small asymmetry between left and right junctions. The spectroscopy of SQUID *R16* is shown in Fig. 12 as a function of φ_X at two values of

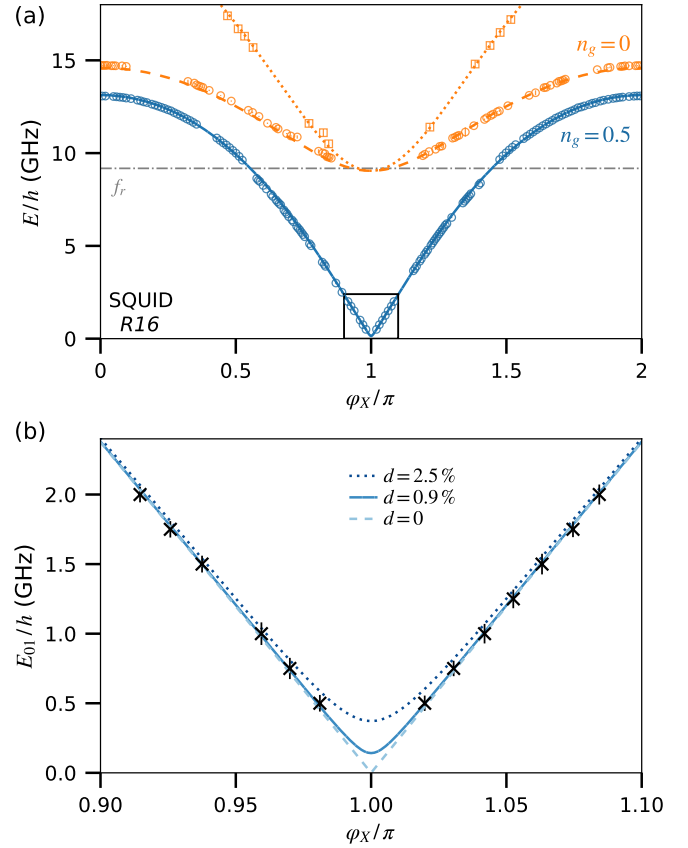


FIG. 12. SQUID *R16* energy transitions as a function of reduced flux φ_X extracted from two-tone spectroscopy measurements. (a) The transition f_{01} is measured at charge offset $n_g = 0.5$ (blue circles along solid lines) and $n_g = 0$ (orange circles along dashed lines). The transition f_{02} is measured at $n_g = 0$ (orange squares along dotted line) and is out of the measurement range at $n_g = 0.5$. Error bars indicate measured full-width half maximum of transitions, and lines are best fits to the data using the BiSQUID Hamiltonian with $\beta = 0$. The resonator bare frequency $f_r = 9.178$ GHz is indicated by a gray dash-dot line. (b) Zoom on the f_{01} transition at $n_g = 0.5$ around $\varphi_X = \pi$. The best fit of the data yields the asymmetry parameter $d = (\alpha - 1)/(\alpha + 1) = 0.9\%$ (solid line). Other two lines show simulations for an upper bound of the asymmetry of $d = 2.5\%$ (dotted line) and a fully symmetric SQUID with $d=0$ (dashed line).

n_g . At $n_g = 0$, we measured the first two transitions f_{01} (orange circles) and f_{02} (orange squares). They converge to a similar value at $\varphi_X = \pi$. However we cannot resolve the transitions near this point because it is almost resonant with the readout resonator frequency f_r (gray dash-dot line). The first transition f_{01} is also measured at $n_g = 0.5$, and a zoom down to 0.5 GHz is shown in Fig. 12(b). Similarly to the BiSQUIDs, the spectral line of f_{01} disappears near $\varphi_X = \pi$ because of thermal effects and because of the decrease of the charge-coupled resonator shift.

We fit the transitions to the eigenenergies of the BiSQUID Hamiltonian Eq. (3) with $\beta = 0$. We use

three free parameters: the Josephson energy E_j , the charging energy E_C and the asymmetry parameter $d = (\alpha - 1)/(\alpha + 1)$. The best fit parameters are given in Table I and the simulated energy levels are shown in Fig. 12. We find an asymmetry parameter of $d = 0.9\%$. Additional simulated energy levels are shown in Fig. 12(b) for an upper bound of the asymmetry of $d = 2.5\%$ and for a fully symmetric SQUID with $d = 0$. Measuring f_{01} down to lower frequencies would be required to further constrain the asymmetry parameter.

ACKNOWLEDGMENTS

We thank Jean-Noël Fuchs for elucidating the analogy to topological semimetals. We thank Jeffrey Teo, Roman Riwar, Valla Fatemi, Joël Griesmar, Hugues Pothier, Landry Bretheau, Benoît Douçot, and Benjamin Wieder for discussions. This project has received funding from the European Research Council (ERC) under the European Union’s Horizon 2020 research and innovation programme (grant agreement 636744). The research was also supported by Japanese Society for the Promotion of Science International Research Fellowship L22559, IDEX Grant No. ANR-10-IDEX-0001-02 PSL, a Paris “Programme Emergence(s)” Grant, the Office of Naval Research under Award No. N00014-20-1-2356, and the Thomas Jefferson Fund, a program of FACE Foundation launched in collaboration with the French Embassy. We thank IARPA and MIT Lincoln Labs for providing a TWPA and ESPCI Paris for providing SEM services.

-
- [1] D. Thouless, *Topological quantum numbers in nonrelativistic physics* (World Scientific, 1998).
- [2] K. von Klitzing, T. Chakraborty, P. Kim, V. Madhavan, X. Dai, J. McIver, Y. Tokura, L. Savary, D. Smirnova, A. M. Rey, C. Felser, J. Gooth, and X. Qi, 40 years of the quantum Hall effect, *Nature Reviews Physics* **2**, 397 (2020).
- [3] M. V. Berry and M. Wilkinson, Diabolical points in the spectra of triangles, *Proceedings of the Royal Society of London. A. Mathematical and Physical Sciences* **392**, 15 (1984).
- [4] J. Wang and S.-C. Zhang, Topological states of condensed matter, *Nature Materials* **16**, 1062 (2017), number: 11 Publisher: Nature Publishing Group.
- [5] R. Moessner and J. E. Moore, *Topological Phases of Matter* (Cambridge University Press, 2021).
- [6] H. Scherer and B. Camarota, Quantum metrology triangle experiments: A status review, *Measurement Science and Technology* **23**, 124010 (2012).
- [7] J. Brun-Picard, S. Djordjevic, D. Leprat, F. Schopfer, and W. Poirier, Practical Quantum Realization of the Ampere from the Elementary Charge, *Physical Review X* **6**, 041051 (2016).
- [8] A. Gyenis, A. Di Paolo, J. Koch, A. Blais, A. A. Houck, and D. I. Schuster, Moving beyond the Transmon: Noise-Protected Superconducting Quantum Circuits, *PRX Quantum* **2**, 030101 (2021).
- [9] C.-K. Chiu, J. C. Y. Teo, A. P. Schnyder, and S. Ryu, Classification of topological quantum matter with symmetries, *Reviews of Modern Physics* **88**, 035005 (2016).
- [10] A. Garg, Berry phases near degeneracies: Beyond the simplest case, *American Journal of Physics* **78**, 661 (2010).
- [11] K. Satzinger, Y.-J. Liu, A. Smith, C. Knapp, M. Newman, N. C. Jones, Z. Chen, C. Quintana, X. Mi, A. Dunsworth, C. Gidney, I. Aleiner, F. Arute, K. Arya, A. Atalaya, R. Babbush, J. C. Bardin, R. Barends, J. Basso, A. Bengtsson, A. Bilmes, M. Broughton, B. B. Buckley, D. A. Buell, B. Burkett, N. Bushnell, B. Chiaro, R. Collins, W. Courtney, S. Demura, A. R. Derk, D. Eppens, C. Erickson, L. Faoro, E. Farhi, B. Foxen, M. Giustina, A. Greene, J. A. Gross, M. P. Harrigan, S. D. Harrington, J. Hilton, S. Hong, T. Huang, W. J. Huggins, L. B. Ioffe, S. V. Isakov, E. Jeffrey, Z. Jiang, D. Kafri, K. Kechedzhi, T. Khattar, S. Kim, P. V. Klimov, A. N. Korotkov, F. Kostritsa, D. Landhuis, P. Laptev, A. Locharla, E. Lucero, O. Martin, J. R. McClean, M. McEwen, K. C. Miao, M. Mohseni, S. Montazeri, W. Mruczkiewicz, J. Mutus, O. Naaman, M. Neeley, C. Neill, M. Y. Niu, T. E. O'Brien, A. Opremcak, B. Pato, A. Petukhov, N. C. Rubin, D. Sank, V. Shvarts, D. Strain, M. Szalay, B. Villalonga, T. C. White, Z. Yao, P. Yeh, J. Yoo, A. Zalcman, H. Neven, S. Boixo, A. Megrant, Y. Chen, J. Kelly, V. Smelyanskiy, A. Kitaev, M. Knap, F. Pollmann, and P. Roushan, Realizing topologically ordered states on a quantum processor, *Science* **374**, 1237 (2021).
- [12] U. Vool and M. Devoret, Introduction to quantum electromagnetic circuits, *International Journal of Circuit Theory and Applications* **45**, 897 (2017).
- [13] J. E. Avron, A. Raveh, and B. Zur, Quantum Conductance in Networks, *Physical Review Letters* **58**, 2110 (1987).
- [14] J. E. Avron, A. Raveh, and B. Zur, Adiabatic quantum transport in multiply connected systems, *Reviews of Modern Physics* **60**, 873 (1988).
- [15] J. E. Avron and M. C. Cross, Integer charge transport in Josephson junctions, *Physical Review B* **39**, 756 (1989).
- [16] J. P. Pekola, J. J. Toppari, M. Aunola, M. T. Savolainen, and D. V. Averin, Adiabatic transport of Cooper pairs in arrays of Josephson junctions, *Physical Review B* **60**, R9931 (1999), arXiv:cond-mat/9904264.
- [17] M. Aunola and J. J. Toppari, Connecting Berry's phase and the pumped charge in a Cooper pair pump, *Physical Review B* **68**, 020502(R) (2003).
- [18] M. Mottonen, J. P. Pekola, J. J. Vartiainen, V. Brosco, and F. W. J. Hekking, Measurement scheme of the Berry phase in superconducting circuits, *Physical Review B* **73**, 214523 (2006), arXiv:cond-mat/0604198.
- [19] M. Mottonen, J. J. Vartiainen, and J. P. Pekola, Experimental determination of the Berry phase in a superconducting charge pump, *Physical Review Letters* **100**, 177201 (2008), arXiv:0710.5623.
- [20] R. Leone, L. P. Lévy, and P. Lafarge, The Cooper Pair Pump as a Quantized Current Source, *Physical Review Letters* **100**, 117001 (2008), arXiv:0711.0210.
- [21] R. Leone and L. Lévy, Topological quantization by controlled paths: Application to Cooper pairs pumps, *Physical Review B* **77**, 064524 (2008), arXiv:0711.0586.
- [22] P. A. Erdman, F. Taddei, J. T. Peltonen, R. Fazio, and J. P. Pekola, Fast and accurate Cooper pair pump, *Physical Review B* **100**, 235428 (2019), arXiv:1909.13627.
- [23] T. Herrig and R.-P. Riwar, Cooper-pair transistor as a minimal topological quantum circuit, *Physical Review Research* **4**, 013038 (2022).
- [24] L. Peyruchat, J. Griesmar, J.-D. Pillet, and Ç. Ö. Girit, Transconductance quantization in a topological Josephson tunnel junction circuit, *Physical Review Research* **3**, 013289 (2021).
- [25] V. Fatemi, A. R. Akhmerov, and L. Bretheau, Weyl Josephson circuits, *Physical Review Research* **3**, 013288 (2021).
- [26] L. Peralta Gavensky, G. Usaj, and C. A. Balseiro, Multiterminal Josephson junctions: A road to topological flux networks, *Europhysics Letters* **141**, 36001 (2023).
- [27] V. Bouchiat, D. Vion, P. Joyez, D. Esteve, and M. H. Devoret, Quantum coherence with a single Cooper pair, *Physica Scripta* **1998**, 165 (1998), publisher: IOP Publishing.
- [28] Y. Nakamura, Y. A. Pashkin, and J. S. Tsai, Coherent control of macroscopic quantum states in a single-Cooper-pair box, *Nature* **398**, 786 (1999), number: 6730 Publisher: Nature Publishing Group.
- [29] M. Robnik and M. V. Berry, False time-reversal violation and energy level statistics: the role of anti-unitary symmetry, *Journal of Physics A: Mathematical and General* **19**, 669 (1986).
- [30] Y. Aharonov, S. Coleman, A. S. Goldhaber, S. Nussinov, S. Popescu, B. Reznik, D. Rohrlich, and L. Vaidman, Aharonov-Bohm and Berry Phases for a Quantum Cloud of Charge, *Physical Review Letters* **73**, 918

- (1994), publisher: American Physical Society.
- [31] F. E. Meijer, A. F. Morpurgo, and T. M. Klapwijk, One-dimensional ring in the presence of Rashba spin-orbit interaction: Derivation of the correct Hamiltonian, *Physical Review B* **66**, 033107 (2002).
- [32] Q. H. Liu and T. G. Liu, Quantum Hamiltonian for the Rigid Rotator, *International Journal of Theoretical Physics* **42**, 2877 (2003).
- [33] G. A. Vugalter, A. K. Das, and V. A. Sorokin, A charged particle on a ring in a magnetic field: quantum revivals, *European Journal of Physics* **25**, 157 (2004).
- [34] H. Nicolai, Supersymmetry and spin systems, *Journal of Physics A: Mathematical and General* **9**, 1497 (1976).
- [35] E. Witten, Dynamical breaking of supersymmetry, *Nuclear Physics B* **188**, 513 (1981).
- [36] A. Lahiri, P. K. Roy, and B. Bagchi, Supersymmetry in quantum mechanics, *International Journal of Modern Physics A* **05**, 1383 (1990), publisher: World Scientific Publishing Co.
- [37] F. Cooper, A. Khare, and U. Sukhatme, Supersymmetry and quantum mechanics, *Physics Reports* **251**, 267 (1995).
- [38] A. R. P. Rau, Supersymmetry in quantum mechanics: An extended view, *Journal of Physics A: Mathematical and General* **37**, 10421 (2004).
- [39] F. Correa and M. S. Plyushchay, Hidden supersymmetry in quantum bosonic systems, *Annals of Physics* **322**, 2493 (2007).
- [40] V. Jakubský, L.-M. Nieto, and M. S. Plyushchay, The origin of the hidden supersymmetry, *Physics Letters B* **692**, 51 (2010).
- [41] V. A. Andreev and P. B. Lerner, Supersymmetry in the Jaynes-Cummings model, *Physics Letters A* **134**, 507 (1989).
- [42] J. Behrends and B. Béri, Supersymmetry in the Standard Sachdev-Ye-Kitaev Model, *Physical Review Letters* **124**, 236804 (2020).
- [43] T. Grover, D. N. Sheng, and A. Vishwanath, Emergent Space-Time Supersymmetry at the Boundary of a Topological Phase, *Science* **344**, 280 (2014).
- [44] P.-L. Zhao and G.-Z. Liu, Merging diabolical points of a superconducting circuit, *npj Quantum Materials* **4**, 1 (2019).
- [45] M.-L. Cai, Y.-K. Wu, Q.-X. Mei, W.-D. Zhao, Y. Jiang, L. Yao, L. He, Z.-C. Zhou, and L.-M. Duan, Observation of supersymmetry and its spontaneous breaking in a trapped ion quantum simulator, *Nature Communications* **13**, 3412 (2022).
- [46] J. Ulrich, D. Otten, and F. Hassler, Simulation of supersymmetric quantum mechanics in a Cooper-pair box shunted by a Josephson rhombus, *Physical Review B* **92**, 245444 (2015).
- [47] M. Combescure, F. Gieres, and M. Kibler, Are $N = 1$ and $N = 2$ supersymmetric quantum mechanics equivalent?, *Journal of Physics A: Mathematical and General* **37**, 10385 (2004).
- [48] J. von Neuman and E. Wigner, Über merkwürdige diskrete Eigenwerte. Über das Verhalten von Eigenwerten bei adiabatischen Prozessen, *Physikalische Zeitschrift* **30**, 467 (1929).
- [49] J. Griesmar, *A mesoscopic spectrometer based on the Josephson effect*, Theses, Université Paris sciences et lettres (2018).
- [50] H. Weisbrich, M. Bestler, and W. Belzig, Tensor Monopoles in superconducting systems, *Quantum* **5**, 601 (2021).
- [51] X. Feng, J. Zhu, W. Wu, and S. A. Yang, Two-dimensional topological semimetals, *Chinese Physics B* **30**, 107304 (2021), arxiv:2103.13772 [cond-mat].
- [52] J. L. Mañes, F. Guinea, and M. A. H. Vozmediano, Existence and topological stability of Fermi points in multilayered graphene, *Physical Review B* **75**, 155424 (2007), arxiv:cond-mat/0611347.
- [53] A. Blais, A. L. Grimsmo, S. M. Girvin, and A. Wallraff, Circuit quantum electrodynamics, *Reviews of Modern Physics* **93**, 025005 (2021).
- [54] L. Glazman and G. Catelani, Bogoliubov quasiparticles in superconducting qubits, *SciPost Physics Lecture Notes*, 031 (2021).
- [55] A. P. Vepsäläinen, A. H. Karamlou, J. L. Orrell, A. S. Dogra, B. Loer, F. Vasconcelos, D. K. Kim, A. J. Melville, B. M. Niedzielski, J. L. Yoder, S. Gustavsson, J. A. Formaggio, B. A. VanDevender, and W. D. Oliver, Impact of ionizing radiation on superconducting qubit coherence, *Nature* **584**, 551 (2020).
- [56] M. McEwen, L. Faoro, K. Arya, A. Dunsworth, T. Huang, S. Kim, B. Burkett, A. Fowler, F. Arute, J. C. Bardín, A. Bengtsson, A. Bilmes, B. B. Buckley, N. Bushnell, Z. Chen, R. Collins, S. Demura, A. R. Derk, C. Erickson, M. Giustina, S. D. Harrington, S. Hong, E. Jeffrey, J. Kelly, P. V. Klimov, F. Kostritsa, P. Laptev, A. Locharla, X. Mi, K. C. Miao, S. Montazeri, J. Mutus, O. Naaman, M. Neeley, C. Neill, A. Opremcak, C. Quintana, N. Redd, P. Roushan, D. Sank, K. J. Satzinger, V. Shvarts, T. White, Z. J. Yao, P. Yeh, J. Yoo, Y. Chen, V. Smelyanskiy, J. M. Martinis, H. Neven, A. Megrant, L. Ioffe, and R. Barends, Resolving catastrophic error bursts from cosmic rays in large arrays of superconducting qubits, *Nature Physics* 10.1038/s41567-021-01432-8 (2021), arXiv:2104.05219.
- [57] L. Cardani, F. Valenti, N. Casali, G. Catelani, T. Charpentier, M. Clemenza, I. Colantoni, A. Cruciani, G. D'Imperio, L. Gironi, L. Grünhaupt, D. Gusenkova, F. Henriques, M. Lagoin, M. Martinez, G. Pettinari, C. Rusconi, O. Sander, C. Tomei, A. V. Ustinov, M. Weber, W. Wernsdorfer, M. Vignati, S. Pirro, and I. M. Pop, Reducing the impact of radioactivity on quantum circuits in a deep-underground facility, *Nature Communications* **12**, 2733 (2021).
- [58] R. T. Gordon, C. E. Murray, C. Kurter, M. Sandberg, S. A. Hall, K. Balakrishnan, R. Shelby, B. Wacaser, A. A. Stabile, J. W. Sleight, M. Brink, M. B. Rothwell, K. Rodbell, O. Dial, and M. Steffen, Environmental Radiation Impact on Lifetimes and Quasiparticle Tunneling Rates of Fixed-Frequency Transmon Qubits, arXiv:2105.14003 [quant-ph] (2021), arXiv:2105.14003 [quant-ph].
- [59] T. Connolly, P. D. Kurilovich, S. Diamond, H. Nho, C. G. L. Bøttcher, L. I. Glazman, V. Fatemi, and M. H. Devoret, Coexistence of nonequilibrium density and equilibrium energy distribution of quasiparticles in a superconducting qubit (2023), arxiv:2302.12330 [cond-mat, physics:quant-ph].
- [60] S. Park, C. Metzger, L. Tosi, M. F. Goffman, C. Urbina, H. Pothier, and A. L. Yeyati, From adiabatic to dispersive readout of quantum circuits, *Physical Review Letters* **125**, 077701 (2020), arxiv:2007.05030 [cond-mat,

- physics:quant-ph].
- [61] L. Fu and C. L. Kane, Topological insulators with inversion symmetry, *Physical Review B* **76**, 045302 (2007).
- [62] G. E. Volovik, Quantum Phase Transitions from Topology in Momentum Space, in *Quantum Analogues: From Phase Transitions to Black Holes and Cosmology*, Vol. 718, edited by W. G. Unruh and R. Schützhold (Springer Berlin Heidelberg, Berlin, Heidelberg, 2007) pp. 31–73.
- [63] S. Y. Zhou, G.-H. Gweon, A. V. Fedorov, P. N. First, W. A. de Heer, D.-H. Lee, F. Guinea, A. H. Castro Neto, and A. Lanzara, Substrate-induced bandgap opening in epitaxial graphene, *Nature Materials* **6**, 770 (2007).
- [64] S. Y. Zhou, D. A. Siegel, A. V. Fedorov, F. E. Gabaly, A. K. Schmid, A. H. C. Neto, D.-H. Lee, and A. Lanzara, Origin of the energy bandgap in epitaxial graphene, *Nature Materials* **7**, 259 (2008).
- [65] E. Rotenberg, A. Bostwick, T. Ohta, J. L. McChesney, T. Seyller, and K. Horn, Origin of the energy bandgap in epitaxial graphene, *Nature Materials* **7**, 258 (2008).
- [66] T. Herrig, J. H. Pixley, E. J. König, and R.-P. Riwar, Quasiperiodic circuit quantum electrodynamics, *npj Quantum Information* **9**, 1 (2023).
- [67] D. Willsch, D. Rieger, P. Winkel, M. Willsch, C. Dickel, J. Krause, Y. Ando, R. Lescanne, Z. Leghtas, N. T. Bromm, P. Deb, O. Lanes, Z. K. Mineev, B. Dening, S. Geisert, S. Günzler, S. Ihssen, P. Paluch, T. Reisinger, R. Hanna, J. H. Bae, P. Schüffelgen, D. Grützmacher, L. Buimaga-Iarinca, C. Morari, W. Wernsdorfer, D. P. DiVincenzo, K. Michielsen, G. Catelani, and I. M. Pop, Observation of josephson harmonics in tunnel junctions (2023), arXiv:2302.09192 [quant-ph].
- [68] G. Pintér, G. Frank, D. Varjas, and A. Pályi, Birth quota of non-generic degeneracy points (2022), arXiv:2202.05825 [cond-mat.mes-hall].
- [69] D. M. Berns, M. S. Rudner, S. O. Valenzuela, K. K. Berggren, W. D. Oliver, L. S. Levitov, and T. P. Orlando, Amplitude spectroscopy of a solid-state artificial atom, *Nature* **455**, 51 (2008).
- [70] N. Maleeva, L. Grünhaupt, T. Klein, F. Levy-Bertrand, O. Dupre, M. Calvo, F. Valenti, P. Winkel, F. Friedrich, W. Wernsdorfer, A. V. Ustinov, H. Rotzinger, A. Monfardini, M. V. Fistul, and I. M. Pop, Circuit quantum electrodynamics of granular aluminum resonators, *Nature Communications* **9**, 3889 (2018).
- [71] V. Gritsev and A. Polkovnikov, Dynamical quantum Hall effect in the parameter space, *Proceedings of the National Academy of Sciences* **109**, 6457 (2012).
- [72] T. Ozawa and N. Goldman, Probing localization and quantum geometry by spectroscopy, *Physical Review Research* **1**, 032019(R) (2019).
- [73] R. L. Klees, G. Rastelli, J. C. Cuevas, and W. Belzig, Microwave Spectroscopy Reveals the Quantum Geometric Tensor of Topological Josephson Matter, *Physical Review Letters* **124**, 197002 (2020).
- [74] S. Das Sarma, J. D. Sau, and T. D. Stanescu, Splitting of the zero-bias conductance peak as smoking gun evidence for the existence of the Majorana mode in a superconductor-semiconductor nanowire, *Phys. Rev. B* **86**, 220506(R) (2012).
- [75] S. M. Frolov, P. Zhang, B. Zhang, Y. Jiang, S. Byard, S. R. Mudi, J. Chen, A. H. Chen, M. Hocevar, M. Gupta, C. Riggert, and V. S. Pribiag, "smoking gun" signatures of topological milestones in trivial materials by measurement fine-tuning and data postselection (2023), arXiv:2309.09368 [cond-mat.mes-hall].
- [76] L. Peyruchat, *Topological phenomena in Josephson tunnel junction circuits*, Ph.D. thesis, Physique en Île-de-France, Collège de France (2022).
- [77] A. Monjou and R. Leone, Merging diabolical points of a superconducting circuit, *Condensed Matter Physics* **16**, 33801 (2013), arxiv:1111.3671.
- [78] G. Frank, D. Varjas, G. Pintér, and A. Pályi, Weyl-point teleportation (2022), arxiv:2112.14556 [cond-mat].
- [79] H. Weisbrich, M. Bestler, and W. Belzig, Tensor Monopoles in superconducting systems, *Quantum* **5**, 601 (2021).
- [80] O. Foda, A supersymmetric phase transition in Josephson-tunnel-junction arrays, *Nuclear Physics B* **300**, 611 (1988).
- [81] L. Bretheau, C. O. Girit, H. Pothier, D. Esteve, and C. Urbina, Exciting Andreev pairs in a superconducting atomic contact, *Nature* **499**, 312 (2013).
- [82] A. Zazunov, V. S. Shumeiko, E. N. Bratus', J. Lantz, and G. Wendin, Andreev Level Qubit, *Physical Review Letters* **90**, 087003 (2003).
- [83] C. Janvier, L. Tosi, L. Bretheau, Ç. Ö. Girit, M. Stern, P. Bertet, P. Joyez, D. Vion, D. Esteve, M. F. Goffman, H. Pothier, and C. Urbina, Coherent manipulation of Andreev states in superconducting atomic contacts, *Science* **349**, 1199 (2015).
- [84] L. Tosi, C. Metzger, M. F. Goffman, C. Urbina, H. Pothier, S. Park, A. L. Yeyati, J. Nygård, and P. Krogstrup, Spin-Orbit Splitting of Andreev States Revealed by Microwave Spectroscopy, *Physical Review X* **9**, 011010 (2019).
- [85] M. Hays, V. Fatemi, D. Bouman, J. Cerrillo, S. Diamond, K. Serniak, T. Connolly, P. Krogstrup, J. Nygård, A. Levy Yeyati, A. Geresdi, and M. H. Devoret, Coherent manipulation of an Andreev spin qubit, *Science* **373**, 430 (2021).
- [86] B. van Heck, S. Mi, and A. R. Akhmerov, Single fermion manipulation via superconducting phase differences in multi-terminal Josephson junctions, arXiv:1408.1563 [cond-mat] (2014), arxiv:1408.1563 [cond-mat].
- [87] R.-P. Riwar, M. Houzet, J. S. Meyer, and Y. V. Nazarov, Multi-terminal Josephson junctions as topological matter, *Nature Communications* **7**, 11167 (2016).
- [88] A. V. Galaktionov, Supersymmetric Hamiltonian solutions simulated by Andreev bound states, *Physical Review B* **101**, 134501 (2020).
- [89] X. Chen, Z.-C. Gu, Z.-X. Liu, and X.-G. Wen, Symmetry protected topological orders and the group cohomology of their symmetry group, *Physical Review B* **87**, 155114 (2013).
- [90] B. Zeng, X. Chen, D.-L. Zhou, and X.-G. Wen, Symmetry-Protected Topological Phases, in *Quantum Information Meets Quantum Matter: From Quantum Entanglement to Topological Phases of Many-Body Systems*, Quantum Science and Technology, edited by B. Zeng, X. Chen, D.-L. Zhou, and X.-G. Wen (Springer, New York, NY, 2019) pp. 281–332.
- [91] I. L. Egusquiza, A. Iñiguez, E. Rico, and A. Villarino, Role of anomalous symmetry in π qubits, *Physical Review B* **105**, L201104 (2022).
- [92] P. A. Erdman, F. Taddei, J. T. Peltonen, R. Fazio, and

- J. P. Pekola, Fast and accurate Cooper pair pump, *Physical Review B* **100**, 235428 (2019), arxiv:1909.13627.
- [93] H. Weisbrich, R. L. Klees, O. Zilberberg, and W. Belzig, Fractional transconductance via nonadiabatic topological Cooper pair pumping, *Physical Review Research* **5**, 043045 (2023).
- [94] L. B. Ioffe, M. V. Feigel'man, A. Ioselevich, D. Ivanov, M. Troyer, and G. Blatter, Topologically protected quantum bits using Josephson junction arrays, *Nature* **415**, 503 (2002).
- [95] B. Douçot, M. V. Feigel'man, and L. B. Ioffe, Topological Order in the Insulating Josephson Junction Array, *Physical Review Letters* **90**, 107003 (2003).
- [96] S. Gladchenko, D. Olaya, E. Dupont-Ferrier, B. Douçot, L. B. Ioffe, and M. E. Gershenson, Superconducting nanocircuits for topologically protected qubits, *Nature Physics* **5**, 48 (2009).
- [97] R. Usmanov, *Protected Quantum Bits and Josephson Junction Arrays*, Ph.D. thesis, Rutgers University - Graduate School - New Brunswick (2010).
- [98] P. Brookes, T. Chang, M. Szymanska, E. Grosfeld, E. Ginossar, and M. Stern, Protection of Quantum Information in a Chain of Josephson Junctions, *Physical Review Applied* **17**, 024057 (2022).
- [99] G. Falci, R. Fazio, G. M. Palma, J. Siewert, and V. Vedral, Detection of geometric phases in superconducting nanocircuits, *Nature* **407**, 355 (2000).
- [100] P. Solinas, J.-M. Pirkkalainen, and M. Möttönen, Ground-state geometric quantum computing in superconducting systems, *Physical Review A* **82**, 052304 (2010).
- [101] J. Zhang, T. H. Kyaw, S. Filipp, L.-C. Kwek, E. Sjöqvist, and D. Tong, Geometric and holonomic quantum computation, *Physics Reports Geometric and Holonomic Quantum Computation*, **1027**, 1 (2023).
- [102] N. P. Armitage, E. J. Mele, and A. Vishwanath, Weyl and Dirac semimetals in three-dimensional solids, *Reviews of Modern Physics* **90**, 015001 (2018).
- [103] A. Akhmerov, Connecting the dots, <https://quantumtinkerer.tudelft.nl/blog/connecting-the-dots/> (2017).
- [104] Z. K. Mineev, Z. Leghtas, S. O. Mundhada, L. Christakis, I. M. Pop, and M. H. Devoret, Energy-participation quantization of Josephson circuits, *npj Quantum Information* **7**, 1 (2021).
- [105] P. Groszkowski and J. Koch, Scqubits: A Python package for superconducting qubits, *Quantum* **5**, 583 (2021).
- [106] S. P. Chitta, T. Zhao, Z. Huang, I. Mondragon-Shem, and J. Koch, Computer-aided quantization and numerical analysis of superconducting circuits, *New Journal of Physics* **24**, 103020 (2022).
- [107] C. Macklin, K. O'Brien, D. Hover, M. E. Schwartz, V. Bolkhovsky, X. Zhang, W. D. Oliver, and I. Siddiqi, A near-quantum-limited Josephson traveling-wave parametric amplifier, *Science* **350**, 307 (2015).
- [108] C. D. Wilen, S. Abdullah, N. A. Kurinsky, C. Stanford, L. Cardani, G. D'Imperio, C. Tomei, L. Faoro, L. B. Ioffe, C. H. Liu, A. Opremcak, B. G. Christensen, J. L. DuBois, and R. McDermott, Correlated charge noise and relaxation errors in superconducting qubits, *Nature* **594**, 369 (2021).
- [109] R. Barends, J. Wenner, M. Lenander, Y. Chen, R. C. Bialczak, J. Kelly, E. Lucero, P. O'Malley, M. Mariantoni, D. Sank, H. Wang, T. C. White, Y. Yin, J. Zhao, A. N. Cleland, J. M. Martinis, and J. J. A. Baselmans, Minimizing quasiparticle generation from stray infrared light in superconducting quantum circuits, *Applied Physics Letters* **99**, 113507 (2011).
- [110] J. Aumentado, M. W. Keller, J. M. Martinis, and M. H. Devoret, Nonequilibrium Quasiparticles and $2e\Phi_0$ Periodicity in Single-Cooper-Pair Transistors, *Physical Review Letters* **92**, 066802 (2004).
- [111] T. Yamamoto, Y. Nakamura, Yu. A. Pashkin, O. Astafiev, and J. S. Tsai, Parity effect in superconducting aluminum single electron transistors with spatial gap profile controlled by film thickness, *Applied Physics Letters* **88**, 212509 (2006).
- [112] N. A. Court, A. J. Ferguson, and R. G. Clark, Energy gap measurement of nanostructured thin aluminium films for use in single Cooper-pair devices, *Superconductor Science and Technology* **21**, 015013 (2008), arXiv:0706.4150.
- [113] R.-P. Riwar and G. Catelani, Efficient quasiparticle traps with low dissipation through gap engineering, *Physical Review B* **100**, 144514 (2019).
- [114] K. Kalashnikov, W. T. Hsieh, W. Zhang, W.-S. Lu, P. Kamenov, A. Di Paolo, A. Blais, M. E. Gershenson, and M. Bell, Bifluxon: Fluxon-Parity-Protected Superconducting Qubit, *PRX Quantum* **1**, 010307 (2020), arXiv:1910.03769.
- [115] G. Catelani and J. P. Pekola, Using materials for quasiparticle engineering, *Materials for Quantum Technology* **2**, 013001 (2022), arXiv:2107.09695.
- [116] C. Kurter, C. E. Murray, R. T. Gordon, B. B. Wymore, M. Sandberg, R. M. Shelby, A. Eddins, V. P. Adiga, A. D. K. Finck, E. Rivera, A. A. Stabile, B. Trimm, B. Wacaser, K. Balakrishnan, A. Pyzyna, J. Sleight, M. Steffen, and K. Rodbell, Quasiparticle tunneling as a probe of Josephson junction quality and capacitor material in superconducting qubits, arXiv:2106.11488 [cond-mat, physics:quant-ph] (2021), arXiv:2106.11488 [cond-mat, physics:quant-ph].
- [117] C. Wang, C. Axline, Y. Y. Gao, T. Brecht, L. Frunzio, M. H. Devoret, and R. J. Schoelkopf, Surface participation and dielectric loss in superconducting qubits, *Applied Physics Letters* **107**, 162601 (2015), arxiv:1509.01854.